

Evolution of N/O Abundance Ratios and Ionization Parameters from $z \sim 0$ to 2 Investigated by the Direct Temperature Method ^{† ‡}

Takashi Kojima ^{1,2}, Masami Ouchi ^{1,3}, Kimihiko Nakajima ⁴,
Takatoshi Shibuya ¹, Yuichi Harikane ^{1,2}, and Yoshiaki Ono ¹

¹Institute for Cosmic Ray Research, The University of Tokyo, 5-1-5 Kashiwanoha, Kashiwa, Chiba 277-8582, Japan

²Department of Physics, Graduate School of Science, The University of Tokyo, 7-3-1 Hongo, Bunkyo, Tokyo 113-0033, Japan

³Kavli Institute for the Physics and Mathematics of the Universe (WPI), The University of Tokyo, 5-1-5 Kashiwanoha, Kashiwa, Chiba 277-8583, Japan

⁴European Southern Observatory, Karl-Schwarzschild-Strasse 2, D-85748 Garching, b. München, Germany

[†]Some of the data presented herein were obtained at the W.M. Keck Observatory, which is operated as a scientific partnership among the California Institute of Technology, the University of California and the National Aeronautics and Space Administration. The Observatory was made possible by the generous financial support of the W.M. Keck Foundation.

[‡]Based in part on data collected at Subaru Telescope, which is operated by the National Astronomical Observatory of Japan.

*E-mail: tkojima@icrr.u-tokyo.ac.jp

Received 24-Nov-2016; Accepted 24-Feb-2017 (in press)

Abstract

We present N/O abundance ratios, ionization parameters q_{ion} , and oxygen abundance O/H for a total of 41 galaxies (11 individual galaxies and a 30-galaxy stack) including Ly α emitters and Lyman break galaxies at $z \sim 2$, and investigate galaxy evolution from $z \sim 0$ to 2 in conjunction with 208,529 local SDSS galaxies and 9 green pea galaxies (GPs). In contrast with most of the recent studies, we obtain the N/O ratio, q_{ion} , and O/H measurements by direct T_e methods with [O III] $\lambda 4363$ and [O III] $\lambda 1665$ lines. Based on these reliable measurements, we find that there exist $z \sim 2$ galaxies with an excess of N/O falling beyond the local average of N/O–O/H relation, while the majority of the $z \sim 2$ galaxies have the N/O ratios nearly comparable with $z \sim 0$ galaxies in the N/O–stellar mass relation. Our galaxies place the upper limit of N/O ratio $\log(\text{N/O}) \leq -1.26$ on average, suggesting that the N/O ratio evolves, if at all, by < 0.17 dex. Exploiting our reliable measurements free from the N/O– q_{ion} –O/H degeneracies, we identify, for the first time, that $z \sim 2$ galaxies with offsets in the BPT diagram indicate either 1) only an N/O excess, 2) only a q_{ion} excess, or 3) both N/O and q_{ion} excesses. We argue that the BPT offsets at $z \sim 2$ are not made by one of 1)–3) galaxy populations alone, but the composite of 1)–3) populations. We confirm that these 1)–3) populations also exist at $z \sim 0$, such as GPs and SDSS low-mass and high-SFR galaxies (LMHSs).

Key words: galaxies: abundances — galaxies: evolution — galaxies: high-redshift — galaxies: ISM

1 INTRODUCTION

The [O III] $\lambda 5007/H\beta$ vs. [N II] $\lambda 6584/H\alpha$ diagram, often referred to as the Baldwin–Phillips–Terlevich (BPT Baldwin et al. 1981) diagram, is used to distinguish star-forming galaxies (SFGs) from active galactic nuclei (AGNs). Local SFGs make a tight relation in the BPT diagram, which is caused by the anti-correlation between the oxygen abundance, $12+\log(O/H)$, and the ionization parameter, q_{ion} (Dopita & Evans 1986; Dopita et al. 2000, 2006a). Recent studies have revealed that $z \sim 2$ galaxies have [N II] $\lambda 6584/H\alpha$ (N2) values higher than those of the local SFGs for a given [O III] $\lambda 5007/H\beta$ (O3) on average (Shapley et al. 2005; Erb et al. 2006; Brinchmann et al. 2008; Liu et al. 2008; Kewley et al. 2013b; Steidel et al. 2014; Masters et al. 2014; Yabe et al. 2014; Hayashi et al. 2015; Shapley et al. 2015; Sanders et al. 2016; Kashino et al. 2017). The $z=2$ galaxies observed in the Keck Baryonic Structure Survey (KBSS; Steidel et al. 2014) show the average of ~ 0.4 dex excesses in [N II] $\lambda 6584/H\alpha$. These differences between the local and high- z SFGs are called “BPT offsets”.

The BPT offset indicates the evolution of the physical conditions of the interstellar medium (ISM) in galaxies from $z \sim 0$ to $z \sim 2$. To explain the BPT offset, there are four possible scenarios of galaxy evolution towards $z \sim 2$: high electron densities n_e , high nitrogen-to-oxygen abundance ratios N/O, high ionization parameters, and hard far-ultra violet (FUV) radiation fields. Photoionization models suggest that the BPT offsets appear, if, at least, one of the four parameters is changed from values of typical local galaxies (e.g. Kewley et al. 2013a; Steidel et al. 2014; Sanders et al. 2016).

For the explanation of the n_e redshift evolution, the typical n_e values of $z = 2-3$ SFGs are estimated with [O II] $\lambda\lambda 3727/3729$ and/or [S II] $\lambda\lambda 6716/6731$ ratios to be $n_e \sim 250 \text{ cm}^{-3}$ (Steidel et al. 2014; Shimakawa et al. 2015; Sanders et al. 2016). This n_e value at $z = 2-3$ is about an order of magnitude higher than the typical value of local galaxies, $n_e \sim 25 \text{ cm}^{-3}$, which is derived by Sanders et al. (2016) from the sample of the Sloan Digital Sky Survey (SDSS; York et al. 2000). Although there is a large difference of the n_e values between $z = 2-3$ and local SFGs, photoionization models indicate that this n_e difference can increase [O III] $\lambda 5007/H\beta$ and [N II] $\lambda 6584/H\alpha$ values only by $\sim 0.01, 0.05$, and 0.1 dex for SFGs with the oxygen abundances of $12+\log(O/H)=8.0, 8.3$, and 8.5 , respectively (Sanders et al. 2016). These small changes cannot explain the BPT offset, suggesting that the n_e evolution is not the major source of the BPT offset.

For the explanation of the N/O redshift evolution, Queyrel

et al. (2009), Masters et al. (2014), and Yabe et al. (2015) have estimated N/O ratios at $z \sim 2$, and have claimed the increase of N/O at fixed O/H. The excessive N/O ratios at fixed O/H may be caused by the decrease of O/H due to the pristine gas inflow into galaxies with rich nitrogen gas produced by the secondary nucleosynthesis, while Wolf-Rayet (WR) stars can produce the nitrogen in a time scale shorter than the oxygen production time scale in supernovae (Andrews & Martini 2013). Galaxies with an excessive N/O ratio tend to indicate the WR-star feature in their spectrum (e.g., Pustilnik et al. 2004; Pérez-Montero et al. 2011). Here, Queyrel et al. (2009) and Yabe et al. (2015) have derived the N/O values based on the $z \sim 0$ empirical relation with the ratios of the strong emission lines of [N II] $\lambda 6584/[S II] \lambda\lambda 6716, 6731$ (N2S2). This N2S2 index is calibrated by Pérez-Montero & Contini (2009) and Amorín et al. (2010). Masters et al. (2014) derive the N/O ratio, assuming that the electron temperature (T_e) is 10,000 K. However, with local SDSS galaxies, the strong line method gives N/O values systematically higher than the reliable direct temperature (T_e) method (see Section 5 for more details). Moreover, there remain possible systematics in applying this $z \sim 0$ empirical N2S2 relation to $z \sim 2$ SFGs whose ISM properties should be different from $z \sim 0$ galaxies.

For the explanations of the q_{ion} , Nakajima & Ouchi (2014) have reported that the q_{ion} values of SFGs are systematically higher at $z = 2-3$ than at $z \sim 0$ by an order of magnitude. The values of $12+\log(O/H)$ and q_{ion} are estimated with the combination of the strong line indicators of R_{23} and O_{32} defined as

$$R_{23} \equiv \log \left(\frac{[\text{O II}] \lambda 3727 + [\text{O III}] \lambda\lambda 4959, 5007}{H\beta} \right) \quad (1)$$

$$O_{32} \equiv \log \left(\frac{[\text{O III}] \lambda\lambda 4959, 5007}{[\text{O II}] \lambda 3727} \right), \quad (2)$$

which were introduced by Kobulnicky & Kewley (2004). For the standard H II-region model of a Strömgren sphere, the dependence of q_{ion} on n_e and hydrogen photoionizing photon production rate Q_{H0} is given by $q_{\text{ion}} \propto (Q_{\text{H0}} n_e)^{1/3}$ (Charlot et al. 2001; Shirazi et al. 2014; Nakajima & Ouchi 2014). The factor of 10 evolution in the electron density is not enough to be the major cause of the q_{ion} evolution. Thus, the redshift evolution of q_{ion} would be largely contributed by the increase of the hydrogen photoionizing production rate in galaxies from $z \sim 0$ to $z \sim 2$. The photoionizing rate and the radiation hardness are determined by stellar population properties including stellar age, metallicity, dust extinction, and the initial mass function (IMF). The physical origins of q_{ion} and the radiation hardness largely overlap, and produce similar BPT offsets. In this sense, the

independent determinations of q_{ion} and radiation hardness are challenging in observations, which means the q_{ion} and radiation hardness have a degeneracy. We thus do not investigate the degeneracy of q_{ion} and radiation hardness further in this paper, but instead assume the non-evolving radiation hardness.

Because the n_e evolution cannot explain the BPT offset under the assumption of the non-evolving radiation hardness, in this study, we investigate the remaining two possibilities, the evolution of N/O and q_{ion} . Our goal is to understand the N/O and q_{ion} values of $z \sim 2$ galaxies based on the direct T_e method. We use multiple line ratios including [O III] $\lambda 4363$ and O III] $\lambda\lambda 1661, 1666$ for the reliable T_e method to derive $12+\log(\text{O}/\text{H})$, N/O, and q_{ion} values that are free from many of the systematic uncertainties explained above. For observational data of this study, we conducted rest-frame infra-red (IR) spectroscopy targeting a $z \sim 2$ Ly α emitter (LAE), COSMOS 12805, which has a significant detection of the O III] $\lambda\lambda 1661, 1666$ lines useful for the direct T_e method estimates (Shibuya et al. 2014). We also use ten $z \sim 2 - 3$ galaxies with [O III] $\lambda 4363$ or O III] $\lambda\lambda 1661, 1666$ measurements from the literature and the composite spectrum made of thirty $z \sim 2$ galaxies by Steidel et al. (2016).

The outline of this paper is as follows. In Section 2, we describe our data and observations of COSMOS 12805. Section 3 presents our sample of $z \sim 2$ galaxies, and discusses the reliability of the galaxies in our sample. In Section 4, we explain the measurements of T_e , O/H, N/O, and q_{ion} of the galaxies in our sample. In Section 5, we discuss three relations of N/O– M_* , N/O–O/H, and q_{ion} –O/H for the $z \sim 2$ galaxies. Here we discuss how these three relations are relevant to the BPT diagram offset. We summarize our results in Section 6. Throughout this paper, magnitudes are on the AB system (Oke & Gunn 1983). We adopt the following cosmological parameters, $(h, \Omega_m, \Omega_\Lambda) = (0.7, 0.3, 0.7)$.

2 DATA AND OBSERVATIONS

One of our sample SFGs, COSMOS 12805, is an LAE at $z = 2.159$ (RA= $10^{\text{h}}00^{\text{m}}15.^{\text{s}}29$, Dec= $+02^{\circ}08'07.''48$). This object is selected by the excess of narrowband NB387 flux in the two color diagram of $B - \text{NB387}$ vs. $u^* - \text{NB387}$ (Nakajima et al. 2012, 2013). Shibuya et al. (2014) have carried out follow-up spectroscopic observations for COSMOS 12805 with the Low Resolution Imaging Spectrometer (LRIS; Oke et al. 1998; Steidel et al. 2004) on the Keck-I telescope, and detected O III] $\lambda\lambda 1661, 1666$ emission lines in the spectrum of COSMOS 12805.

In addition, our observation with the Subaru Fiber Multi Object Spectrograph (FMOS; Kimura et al. 2010) gives constraints on nebular line fluxes of [O II] $\lambda 3727$, H β , and [O III] $\lambda\lambda 4959, 5007$. More recently, our program with the Multi-

Object Spectrometer For Infra-Red Exploration (MOSFIRE; McLean et al. 2010, 2012) on the Keck-I telescope covers emission lines of H α , and [N II] $\lambda 6584$. In this section, we describe these observations and data of the Keck/LRIS, Subaru/FMOS, and Keck/MOSFIRE.

Table 1. Emission Line Fluxes of COSMOS 12805

Line	F(λ) ^a	I(λ) ^a	Instrument
(1)	(2)	(3)	(4)
O III] $\lambda 1661$	1.48 ± 0.37	1.70 ± 0.43	Keck/LRIS
O III] $\lambda 1666$	2.29 ± 0.45	2.63 ± 0.52	Keck/LRIS
N III] $\lambda 1750$	$< 1.28^{\text{b}}$	$< 1.47^{\text{b}}$	Keck/LRIS
[O II] $\lambda 3727$	$< 88.3^{\text{b}}$	$< 98.0^{\text{b}}$	Subaru/FMOS
H β $\lambda 4861$	30.5 ± 9.9	33.2 ± 10.8	Subaru/FMOS
[O III] $\lambda 4959$	57.6 ± 12.9	62.8 ± 14.1	Subaru/FMOS
[O III] $\lambda 5007$	197 ± 8.7	215 ± 9.5	Subaru/FMOS
H α $\lambda 6563$	86.6 ± 1.4	91.8 ± 1.5	Keck/MOSFIRE
[N II] $\lambda 6584$	$< 3.06^{\text{b}}$	$< 3.24^{\text{b}}$	Keck/MOSFIRE

- (1): Emission lines and the rest-frame wavelength. (2): Measured fluxes. (3): Dust-corrected fluxes under the assumption of $E(B - V)_{\text{neb}} = 0.02$ mag that are given by the Balmer decrement measurement (Section 3). (4): Instruments used in our observations.

^a In units of $10^{-18} \text{erg cm}^{-2} \text{s}^{-1}$.

^b 2σ upper limit.

2.1 LRIS Data

The Keck/LRIS observations were carried out in 2012 March 19–21 (UT) with seeing sizes of $1.''0 - 1.''4$ (FWHM). The total exposure time was 24,000 seconds for the mask targeting COSMOS 12805. The spectral resolution is $R \sim 1000$, which corresponds to $\simeq 300 \text{ km s}^{-1}$. Details of our LRIS observations and data reduction are presented in Shibuya et al. (2014).

Figure 1 shows the rest-frame UV spectrum normalized by the UV continuum flux density of COSMOS 12805. The O III] $\lambda 1661$ and O III] $\lambda 1666$ lines (referred to as O III] $\lambda 1665$ line) are detected at signal-to-noise (S/N) ratios of 4.0 and 5.1, respectively. Based on the wavelength interval and the S/N ratios of the two lines, the total O III] $\lambda 1665$ detection confidence level is estimated to be 6.8σ . The fluxes of the O III] $\lambda 1661$ and O III] $\lambda 1666$ emission lines are 0.92×10^{-18} and $1.42 \times 10^{-18} \text{ erg s}^{-1} \text{ cm}^{-2}$, respectively. Here, the fluxes of O III] $\lambda 1661$ and O III] $\lambda 1666$ lines are obtained by Gaussian function fitting. We make a 1-dimensional pixel-noise spectrum based on the data of our LRIS 2-dimensional spectrum where the object is not included, and estimate statistical errors of the line fluxes with the 1-dimensional pixel-noise spectrum in the wavelength range same as the emission-line FWHM.

Although our LRIS slit covered three subcomponents of COSMOS 12805 (see Figure 5 of Shibuya et al. 2014), there exist a non-negligible flux loss due to the large FWHM seeing sizes of $1.''0 - 1.''4$ whose median value is $\simeq 1.''1$. We estimate the slit loss correction factor, F_{LRIS} , with the *Hubble Space Telescope* (HST; Skelton et al. 2014) I_{814} -band image

whose point spread function (PSF) is convolved to match the median seeing size. The F_{LRIS} value is estimated to be 1.61. Applying the LRIS slit loss correction, we obtain 1.48×10^{-18} and $2.29 \times 10^{-18} \text{ erg s}^{-1} \text{ cm}^{-2}$ for the [O III] $\lambda 1661$ and [O III] $\lambda 1666$ emission lines, respectively. Table 1 summarizes the flux estimates of the [O III] emission lines with the F_{LRIS} correction.

2.2 FMOS Data

Our FMOS observations with *J*-long and *H*-short bands were conducted over 2012 December 22–24 (UT) with seeing of $0''.8$ (FWHM). The total exposure times were 2.0 and 6.5 hours for the *J*-long and *H*-short bands, respectively. The spectral resolution of *J*-long and *H*-short bands are $R \simeq 1900$ and 2400, which correspond to 158 and 125 km s^{-1} , respectively. Details of the FMOS observations and data reduction are given in K. Nakajima et al. in preparation.

Figure 2 presents the FMOS spectra of COSMOS 12805. In the *H*-short band spectrum, the [O III] $\lambda 5007$ emission line is detected with an S/N of ~ 23 . The $H\beta$ and [O III] $\lambda 4959$ emission lines are also detected with S/N ratios of $\simeq 3.1$ and 4.5, respectively. The systemic redshift and the emission line fluxes are measured by simultaneous fitting with multiple Gaussian functions to the $H\beta$ and [O III] $\lambda\lambda 4959, 5007$ emission lines. We show the best fit Gaussian functions for $H\beta$ and [O III] $\lambda 4959, 5007$ emission lines in Figure 2. The flux errors are estimated in the same manner as Section 2.1, but with a 1-dimensional pixel-noise spectrum produced with the FMOS pipeline FIBRE-pac (FMOS Image-Based Reduction Package; Iwamura et al. 2012). We obtain a systemic redshift of $z_{\text{sys}} = 2.159$ for COSMOS 12805. The $H\beta$, [O III] $\lambda 4959$, and [O III] $\lambda 5007$ fluxes are 19.2×10^{-18} , 36.2×10^{-18} , and $124 \times 10^{-18} \text{ erg s}^{-1} \text{ cm}^{-2}$, respectively. In contrast, we find no emission line at the expected wavelength of [O II] $\lambda 3727$ in the *J*-long band spectrum. We place a 2σ upper limit on the [O II] $\lambda 3727$ line flux, $< 55.6 \times 10^{-18} \text{ erg s}^{-1} \text{ cm}^{-2}$, assuming that the intrinsic velocity dispersion is 135 km s^{-1} in FWHM. This intrinsic velocity dispersion is estimated with the detected [O III] $\lambda 5007$ emission line.

In the observations for these optical emission lines, the FMOS fiber has covered only one of the three subcomponents in the COSMOS 12805 system. To obtain the total flux for all the three subcomponents, we estimate the flux loss correction factor, F_{FMOS} , for the FMOS $1''.2$ -diameter aperture fiber in the same manner as Section 2.1. Using the *HST* I_{814} -band image whose point-spread function is matched to FWHM= $0''.8$, we measure the flux values for all the three subcomponents and the one covered by the FMOS fiber. The F_{FMOS} value is estimated to be 1.59. Because the morphology of COSMOS 12805 in the I_{814} band can be different from those of *J* and *H* bands for the FMOS data, we make additional calculations for F_{FMOS}

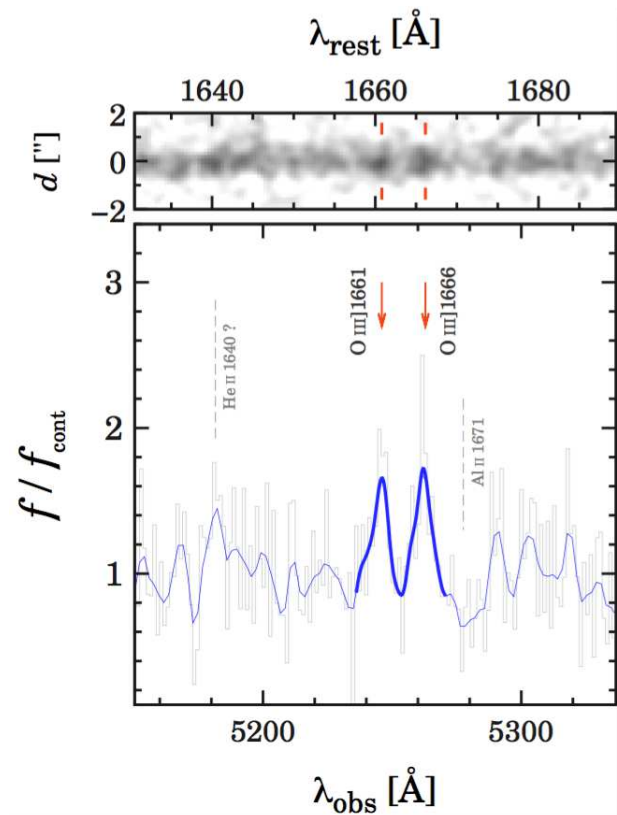


Fig. 1. Rest-frame UV spectrum around the [O III] doublet of COSMOS 12805. The top and bottom panels show the two- and one-dimensional (2D and 1D) spectra, respectively. In the bottom panel, the gray solid line indicates the spectrum normalized to unity in the UV continuum level. The blue solid line presents a spectrum smoothed with a Gaussian function of $\sigma = 3$ pix. The red arrows and the gray vertical dashed lines denote expected wavelengths of inter-stellar emission (i.e. [O III] and He II $\lambda 1640$) and absorption (i.e. Al II $\lambda 1671$) lines for the systemic redshift of $z_{\text{sys}} = 2.159$ (see Section 2.2).

values with the UltraVISTA (McCracken et al. 2012) *J*- and *H*-band images in the $0''.8$ seeing size. The F_{FMOS} value estimated from the *J* band (*H* band) is 10% larger (3% smaller) than the one obtained from the I_{814} band. Although these differences are small, we add these differences to the uncertainties of [O II] $\lambda 3727$, $H\beta$, and [O III] $\lambda\lambda 4959, 5007$ line flux measurements. Applying the FMOS fiber loss correction, we obtain 30.5×10^{-18} for $H\beta$, 57.6×10^{-18} for [O III] $\lambda 4959$, 197×10^{-18} for [O III] $\lambda 5007$, and $< 88.3 \times 10^{-18} \text{ erg s}^{-1} \text{ cm}^{-2}$ for [O II] $\lambda 3727$. Table 1 summarizes the F_{FMOS} -corrected fluxes of the $H\beta$, [O III] $\lambda\lambda 4959, 5007$, and [O II] $\lambda 3727$ emission lines.

2.3 MOSFIRE Observations and Data

We observed COSMOS 12805 with the Keck/MOSFIRE instrument on 2016 January 3 and 4. We carried out *K*-band spectroscopy that covered the wavelength range of $1.95 - 2.4 \mu\text{m}$, targeting the redshifted $H\alpha$ and [N II] $\lambda 6584$ emission lines. We

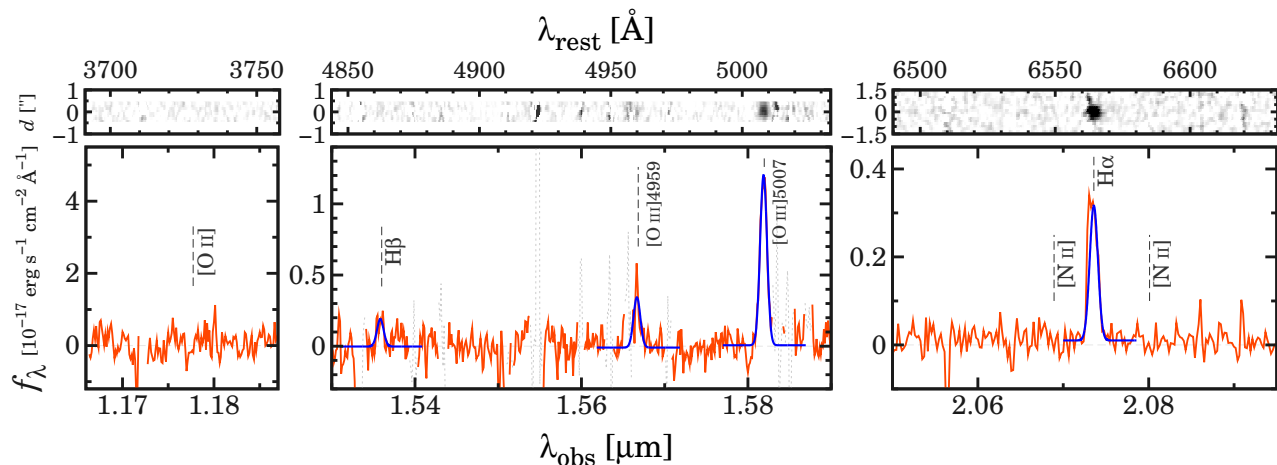


Fig. 2. Rest-frame optical spectra of COSMOS 12805. The left, center, and right panels present the FMOS *J*-long, *H*-short, and MOSFIRE *K*-band spectra, respectively. In each panel, the 2D and 1D spectra are shown at the top and the bottom, respectively. The blue solid lines denote the best-fit Gaussian functions for the detected emission lines. The gray vertical dashed lines indicate expected wavelengths of optical emission lines, [O II], H β , [O III], [N II], and H α for the systemic redshift of $z_{\text{sys}} = 2.159$ (see Section 2.2). The gray dotted lines represent spectra affected by strong OH sky lines.

used the slit width of $0''.7$ and an ABAB dither pattern with individual exposures of 180 seconds. The total integration time was 2.4 hours. The sky conditions were clear throughout the observing run, with an average seeing size of $\text{FWHM} = 0''.6$. The pixel scale was $0''.18$, and the spectral resolution was $R = 3620$ corresponding to $\Delta\lambda \sim 6 \text{ \AA}$ at $\lambda = 2.162 \text{ }\mu\text{m}$. We also took spectra of an A0V-type standard star, HIP 56736, for our flux calibration.

We reduce these data using the MOSFIRE data reduction pipeline.¹ This pipeline performs flat fielding, wavelength calibration, sky subtraction, and cosmic ray removal before producing a combined two-dimensional spectrum. We then extract one-dimensional spectra from the two-dimensional spectra using the IRAF task `blkavg`. We sum the fluxes of a $2''.34$ width (about a $5\times$ the average seeing) at each wavelength bin that covers more than 95% fluxes of the point source along the slit direction. The 3σ limiting flux density is $\simeq 1 \times 10^{-18} \text{ erg s}^{-1} \text{ cm}^{-2} \text{ \AA}^{-1}$ in the wavelength range of 19500–23700 \AA .

The right panel in Figure 2 shows our MOSFIRE spectra at the wavelength of H α and [N II] emission lines. The H α emission line is detected with an S/N of 62. To estimate the total flux, we fit this H α line with a Gaussian function (Figure 2), assuming the systemic redshift of $z_{\text{sys}} = 2.159$. This systemic redshift is determined by the emission lines in the FMOS spectra. In the Gaussian fitting to the H α line, we do not use four spectral pixels in the shorter wavelength side, because these four pixels are contaminated by a strong night sky emission line (Figure 2). The statistical error of the H α line flux is estimated in the same manner as Section 2.1.

Since COSMOS 12805 spatially extends in a direction perpendicular to the slit, we calculate a slit loss correction factor F_{MOSFIRE} to determine total line fluxes. We use the HST I_{814} -band image, and convolve it with a Gaussian kernel to match its PSF to that of the MOSFIRE data. We measure the total and slit-aperture fluxes of COSMOS 12805 on the image, and calculate a correction factor to be $F_{\text{MOSFIRE}} = 2.35$. To evaluate the F_{MOSFIRE} uncertainty raised by morphology differences between the I_{814} and *Ks* bands, we calculate F_{MOSFIRE} values with UltraVISTA (McCracken et al. 2012) *Ks*-band images under the assumption of the $0''.75$ seeing condition. The F_{MOSFIRE} value estimated from the *Ks*-band image is 5% smaller than the one obtained from the I_{814} -band image. We include this difference of the slit loss correction factors to the flux uncertainties of H α and [N II] lines.

The total H α line flux, thus obtained, is $86.6 \times 10^{-18} \text{ erg s}^{-1} \text{ cm}^{-2}$, which is corrected for the slit loss. Since an [N II] emission line is not identified in our MOSFIRE spectra, we estimate a 2σ upper limit on the [N II] line flux to be $3.06 \times 10^{-18} \text{ erg s}^{-1} \text{ cm}^{-2}$ under the assumption of the intrinsic velocity dispersion of 140 km s^{-1} in FWHM. This intrinsic velocity dispersion is estimated with the H α emission line. Table 1 summarizes the flux estimates of the H α and [N II] emission lines after the slit loss correction.

We have thus obtained the LRIS, FMOS, and MOSFIRE data (Sections 2.1–2.3) for COSMOS 12805, which is one of our sample SFGs that are detailed in Section 3.

¹ <https://keck-datareductionpipelines.github.io/MosfireDRP/>

3 SAMPLE

Our sample consists of a total of 41 galaxies, eleven SFGs at $z = 1.4\text{--}3.6$ (Table 2) and the stack of 30 KBSS $z \sim 2$ galaxies taken from Steidel et al. (2016). Hereafter, the stack of 30 KBSS galaxies is dubbed S16-stack, which complements the eleven SFGs. We include the S16-stack in our sample, because Steidel et al. (2016) do not calculate the key quantities of N/O and q_{ion} by the direct T_e method, but the strong line method. Note that we refer to the redshift of the eleven SFGs as $z \sim 2$, because the median redshift of the sample galaxies is 2.2. The O III] $\lambda\lambda 1661, 1666$ or [O III] $\lambda 4363$ emission is detected in each spectrum of the eleven SFGs and the S16-stack (Table 3). One of the eleven SFGs is COSMOS 12805 (Section 2). The other 10 SFGs are taken from the literature: 7 gravitationally lensed galaxies (Fosbury et al. 2003; Villar-Martín et al. 2004; Yuan & Kewley 2009; Christensen et al. 2012b, 2012a; Bayliss et al. 2014; Pettini et al. 2010; James et al. 2014; Stark et al. 2014) and 3 BX galaxies obtained by KBSS (Steidel et al. 2014; Erb et al. 2016). These 10 SFGs are found by our extensive search in the literature with the conditions of the availabilities of O III] $\lambda\lambda 1661, 1666$ / [O III] $\lambda 4363$ and [N II] $\lambda 6584$ / N III] $\lambda 1750$, which are used for the T_e method and the N/O determination, respectively. In this paper, we refer to the eleven galaxies by their IDs that are defined in Tables 2–4.

The nebular line fluxes of the eleven galaxies and the S16-stack are summarized in Table 3 for forbidden and semi-forbidden lines and in Table 4 for Balmer lines. The fluxes are normalized to H β in Tables 3 and 4. Note that all the line fluxes in Tables 3 and 4 are corrected for the telluric absorption, except for ID-2 whose line fluxes corrected for telluric absorption are not available. For ID-2, we estimate that the flux losses by the telluric absorption are 30% for the H α , H β , and [N II] $\lambda 6584$ lines, and 5% for the [O III] $\lambda 5007$ line based on Figure 2 of Christensen et al. (2012b). These flux losses are included in the errors of $T_e(\text{O III})$, $12+\log(\text{O}/\text{H})_{T_e}$, $\log(\text{N}/\text{O})_{T_e}$, and q_{ion} of ID-2. We correct the line fluxes for dust extinction with the Balmer decrement measurements and the extinction curve of Cardelli et al. (1989), using the models of the case B recombination (Osterbrock 1989, Table 5) with $n_e = 100 \text{ cm}^{-3}$ and $T_e \sim 5000\text{--}20000 \text{ K}$ that we derive from the direct T_e methods (Section 4.1). We use the model values of Balmer decrements listed in Table 5 for the three cases of $T_e = 5000, 10000, \text{ and } 20000 \text{ K}$. We apply linear interpolations to obtain model Balmer decrements for our SFGs whose T_e values are $5000\text{--}20000 \text{ K}$. We assume $\text{H}\alpha/\text{H}\beta=2.75$, $\text{H}\gamma/\text{H}\beta=0.475$, and $\text{H}\delta/\text{H}\beta=0.26$ for our SFGs with the measurement of $T_e > 20000 \text{ K}$. The electron temperature of ionized hydrogen, $T_e(\text{H II})$ agrees well with $T_e(\text{O III})$ in our photoionization model calculations with CLOUDY (version 13.03; Ferland et al. 1998, 2013), which are detailed in Section 4. We iteratively perform the dust correction so that the estimated $T_e(\text{O III})$ match the initial assumption of

$T_e(\text{H II})$.

We estimate the color excess $E(B - V)_{\text{neb}}$ with $\text{H}\alpha/\text{H}\beta$, except for ID-2, ID-8, and ID-6. The H α and H β lines of ID-2 are affected by the telluric absorption, and the H α line of ID-8 is not covered in the spectrum. Thus we use $\text{H}\delta/\text{H}\gamma$ and $\text{H}\beta/\text{H}\gamma$ to obtain $E(B - V)_{\text{neb}}$ values of ID-2 and ID-8, respectively. We cannot calculate $E(B - V)_{\text{neb}}$ of the ID-6, because ID-6 only has H β emission.

Table 2 shows physical properties of the eleven galaxies and the S16-stack, which include stellar masses M_* and star-formation rates (SFRs) taken from the literature. The M_* values are obtained by spectral energy distribution (SED) fitting with stellar synthesis models, except for ID-6 and ID-9. The M_* value of ID-6 is estimated with the instantaneous burst models required to reproduce the H β luminosity of ID-6 (Villar-Martín et al. 2004). The M_* value of ID-9 is missing, because there is no M_* measurement in the literature. We choose the Chabrier (2003) IMF in this paper. Because Chabrier or Salpeter (1955) IMF is used to derive M_* in the literature, we subtract 0.20 dex from $\log(M_*/M_\odot)$ of Salpeter IMF to obtain stellar masses of Chabrier IMF (Madau & Dickinson 2014). M_* values of the our $z \sim 2$ galaxies range in $\log(M_*/M_\odot) = 7.49\text{--}10.57$. Their SFRs are $5.7\text{--}906 M_\odot \text{ yr}^{-1}$.

In Table 2, we also present values of rest-frame Ly α equivalent width $\text{EW}_0(\text{Ly}\alpha)$. The six galaxies, ID-1, ID-3, ID-4, ID-5, ID-6, and ID-11, show strong Ly α emission lines. These six galaxies indicate $\text{EW}_0(\text{Ly}\alpha) \gtrsim 20 \text{ \AA}$ and are thus regarded as LAEs.

Table 2. Physical Properties of the $z \sim 2$ Galaxies

ID	Object	z	$\log M_*$ (M_\odot)	SFR ($M_\odot \text{ yr}^{-1}$)	$\text{EW}_0(\text{Ly}\alpha)$ (\AA)	$T_e(\text{OIII})$ (10^4 K)	$12+\log(\text{O}/\text{H})_{T_e}$	$\log(\text{N}/\text{O})_{T_e}$	$\log(q_{\text{ion}})$ (cm s^{-1})	Reliable	Ref.
(1)	(2)	(3)	(4)	(5)	(6)	(7)	(8)	(9)	(10)	(11)	(12)
1	COSMOS 12805	2.159	$9.24^{+0.13}_{-0.17}$	18	33.7 ± 6.0	$1.29^{+0.78}_{-0.09}$	$8.06^{+0.12}_{-0.17}$	$< -1.30^{\dagger}$	$> 7.75^a$	yes	...
2	SMACS 0304	1.963	10.57 ± 0.08	16	$\lesssim 0$	$1.03^{+0.03}_{-0.04}$	$8.36^{+0.06}_{-0.25}$	$-1.57^{+0.18}_{-0.03}$	7.91 ± 0.03	no	1
3	BX74	2.189	9.72^b	58.1^b	101.9 ± 4.4^b	$1.36^{+0.11}_{-0.09}$	8.10 ± 0.08	$-1.26^{+0.11}_{-0.14}$	$8.16^{+0.09}_{-0.10}$	yes	2, 3
4	BX418	2.305	9.45^b	52.0^b	61.8 ± 2.6^b	$1.28^{+0.06}_{-0.05}$	$8.10^{+0.05}_{-0.06}$	$-0.99^{+0.08}_{-0.10}$	$8.20^{+0.04}_{-0.05}$	yes	2, 3
5	BX660	2.174	9.73^b	28.8^b	40.4 ± 2.2^b	1.27 ± 0.07	$8.15^{+0.07}_{-0.06}$	$< -1.39^a$	$8.24^{+0.04}_{-0.05}$	yes	2, 3
6	the Lynx arc	3.357	7.75^c	97	$\sim 480^d$	$1.74^{+0.05}_{-0.04}$	$7.77^{+0.06}_{-0.03}$	$-1.02^{+0.09 \dagger}_{-0.08}$	$> 8.64^a$	no	4, 5
7	Abell 22.3	1.703	8.5 ± 0.2	76	...	$3.01^{+1.18}_{-0.83}$	$7.33^{+0.26}_{-0.22}$	$< -1.74^a$	$7.74^{+0.12}_{-0.09}$	no	6
8	SGAS 1050	3.625	9.5 ± 0.35	84	$\lesssim 0$	$1.05^{+0.03}_{-0.04}$	$8.43^{+0.05}_{-0.04}$	$-1.45^{+0.16 \dagger}_{-0.20}$	$8.55^{+0.04}_{-0.03}$	no	7
9	CSWA 20	1.433	...	5.7	...	$1.41^{+0.22}_{-0.19}$	$7.90^{+0.17}_{-0.14}$	$-1.50^{+0.14}_{-0.18}$	$8.03^{+0.09}_{-0.07}$	yes	8, 9
10	MACS 0451	2.060	7.49	906	...	$2.19^{+0.34}_{-0.36}$	$7.32^{+0.17}_{-0.12}$	$< -1.33^{\dagger}$	$> 8.02^a$	yes	10
11	Abell 860_359	1.702	7.86	55	163.8 ± 25.5	$1.28^{+0.10}_{-0.12}$	$8.06^{+0.12}_{-0.09}$	$< -1.32^{\dagger}$	$> 8.12^a$	yes	10
12	S16-stack	2.396 ± 0.111^e	9.8 ± 0.3^e	29.2 ± 17.6^e	$\sim 4^f$	$1.21^{+0.03}_{-0.04}$	8.17 ± 0.03	-1.21 ± 0.03	7.70 ± 0.02	yes	11

(1): ID. (2): Name of the object. (3): Systemic redshift. (4): Stellar mass. The stellar masses are estimated by SED fitting, except for the ID-6. (5): Star formation rate inferred from the Balmer line and the relation of Kennicutt (1998). (6): Rest-frame equivalent width of a Ly α emission line. (7): Electron temperature of O $^{2+}$. (8): Oxygen abundance derived from the direct T_e methods. (9): Nitrogen to oxygen abundance ratio calculated by the direct T_e methods. (10): Ionization parameter estimated with the [O III]/[O II] line ratio (Kewley & Dopita 2002). (11): *yes* (*no*) indicates that the object is (is not) a galaxy in the reliable sample. (12): Reference. 1: Christensen et al. (2012b, 2012a), 2: Steidel et al. (2014), 3: Erb et al. (2016), 4: Fosbury et al. (2003), 5: Villar-Martín et al. (2004), 6: Yuan & Kewley (2009), 7: Bayliss et al. (2014), 8: Pettini et al. (2010), 9: James et al. (2014), 10: Stark et al. (2014), and 11: Steidel et al. (2016).

^a Upper/Lower limit at the 2σ level.

^b Taken from Erb et al. (2016).

^c Stellar mass estimated with the instantaneous burst model and the H β luminosity measurement (Villar-Martín et al. 2004).

^d We estimate that the continuum level of the Lynx arc is $0.5 \mu\text{Jy}$ at the rest-frame wavelength of the Ly α emission line (Fosbury et al. 2003, Figure 5). The Ly α flux is given in Table 2 of Fosbury et al. (2003). We calculate the $\text{EW}_0(\text{Ly}\alpha)$ value for the Lynx arc, and show the value in this table. Even if we make a conservative estimation of $\text{EW}_0(\text{Ly}\alpha)$ with the continuum level of $3.0 \mu\text{Jy}$, we obtain the rest-frame $\text{EW}_0(\text{Ly}\alpha)$ value of 80\AA .

^e Median values and 1σ scatters of the 30 KBSS galaxies.

^f The $\text{EW}_0(\text{Ly}\alpha)$ value of the S16-stack is estimated with the continuum value of $\sim 0.3 \mu\text{Jy}$ indicated from (Steidel et al. 2016, Figure 2) and the Ly α flux presented in Table 5 of Steidel et al. (2016). The uncertainty of the continuum value does not significantly change the results.

[†] N/O values and upper limits obtained with Equations (10) and (11). The N/O values of the other objects are estimated with Equations (8) and (9).

Table 3. Forbidden and Semi-Forbidden Lines

ID	Object	O III] 1661	O III] 1666	O III] 1661+1666	N III] 1750	[O II] 3727	[O III] 4363	[O III] 4959	[O III] 5007	[O III] 4959+5007	[N II] 6584
(1)	(2)	(3)	(4)	(5)	(6)	(7)	(8)	(9)	(10)	(11)	(12)
1	COSMOS 12805	0.049 ± 0.012	0.075 ± 0.015	0.124 ± 0.019	< 0.042	< 2.90	...	1.89 ± 0.42	6.46 ± 0.29	8.35 ± 0.53	< 0.100
2	SMACS 0304	0.014 ± 0.003	0.023 ± 0.004	0.037 ± 0.007	...	2.10 ± 0.02	...	1.339 ± 0.004 ^a	4.714 ± 0.007 ^d	6.053 ± 0.011 ^a	0.116 ± 0.005 ^a
3	BX74	0.12 ± 0.01	...	1.01 ± 0.04	7.9 ± 1.0	10.37 ± 0.52	0.12 ± 0.03
4	BX418	0.14 ± 0.02	...	0.90 ± 0.03	6.4 ± 0.3	8.7 ± 0.4	0.15 ± 0.03
5	BX660	0.21 ± 0.04	...	0.87 ± 0.04	6.4 ± 0.3	9.6 ± 0.5	< 0.07
6	the Lynx arc	0.56 ± 0.04	0.18 ± 0.02	< 0.25	...	2.58 ± 0.3	7.50 ± 0.3	10.08 ± 0.6	...
7	Abell 22.3	1.11 ± 0.3	0.27 ± 0.10	1.98 ± 0.3	6.45 ± 0.3	8.43 ± 0.6	< 0.050 ^b
8	SGAS 1050	0.018 ± 0.007	0.051 ± 0.007	0.069 ± 0.014	0.014 ± 0.005	0.79 ± 0.02 ^c	< 0.014	2.35 ± 0.02	8.08 ± 0.02	10.43 ± 0.04	...
9	CSWA 20	...	0.10 ± 0.04	0.14 ± 0.06	...	0.99 ± 0.05	...	1.67 ± 0.10	6.64 ± 0.39	6.64 ± 0.39	0.06 ± 0.02
10	MACS 0451	0.2 ± 0.1	0.3 ± 0.1	0.5 ± 0.2	< 0.1	< 0.63	...	1.37 ± 0.05	3.95 ± 0.05	5.31 ± 0.10	< 0.065
11	Abell 860_359	< 0.03	0.083 ± 0.029	0.12 ± 0.04	< 0.03	< 1.2	...	2.03 ± 0.03	6.12 ± 0.10 ^d	8.15 ± 0.13 ^d	...
12	S16-stack	0.009 ± 0.003	0.025 ± 0.003	0.034 ± 0.004	...	2.15 ± 0.04	< 0.06	1.46 ± 0.02	4.37 ± 0.02	5.83 ± 0.02	0.35 ± 0.02

(1): ID. (2): Name of the object. (3)–(12): Forbidden and semi-forbidden line fluxes normalized by the H β flux. The upper limits correspond to the 2 σ levels. The fluxes are *not* corrected for dust extinction.

^a Under the influence of the telluric absorption lines. We do not correct the flux loss by the telluric absorption.

^b Including the potential uncertainty from the low instrumental response at the wavelength.

^c Under the influences of the poor atmospheric throughput and sky lines at the wavelength.

^d [O III] λ 5007 flux estimated from the [O III] λ 4959 flux measurement with the assumption of [O III] λ 5007/ λ 4959 = 3.01 that is self-consistently calculated with our CLOUDY model. [O III] λ 5007 of this object is not detected, due to the strong telluric absorption.

3.1 AGN Activity

Figure 3 presents our galaxies on the BPT diagram. Because the [N II] emission lines are not observed in 3 galaxies of ID-6, ID-8, and ID-10, we only plot the other 8 galaxies here. These 8 galaxies are located in or near the SFG region that is defined by the models of starbursts at $z = 2$ (Kewley et al. 2013a). Although ID-3 is located on the edge of the SFG and AGN regions, the rest-frame UV and optical spectra of ID-3 show no signatures of an AGN (Steidel et al. 2014). We thus regard these 8 galaxies as SFGs with no significant AGN activity. In Figure 3, the [N II]/H α upper limit of ID-7 is very small. This is probably because the [N II] line estimation would include a systematic uncertainty raised by the low throughput spectrum at the wavelength of [N II] (Yuan & Kewley 2009). We find that, at fixed values of [N II]/H α , the majority of our galaxies have the [O III]/H β values that are higher than the $z \sim 0$ SDSS SFG sequence. This trend of the high [O III]/H β values is consistent with those found in previous studies of galaxies at $z \sim 2$ (Shapley et al. 2005; Erb et al. 2006; Liu et al. 2008; Steidel et al. 2014; Shapley et al. 2015).

We then investigate AGN activities of the 3 galaxies, the ID-6, ID-8, and ID-10, which cannot be plotted in the BPT diagram (Figure 3). ID-8 has a spatially extended emission region and no high ionization lines, such as N V λ 1240 and [Ne V] λ 3346, 3426 (Bayliss et al. 2014). Moreover, ID-8 falls on the SFG region of [O II] λ 3727, [Ne III] λ 3869 diagnostic diagram obtained by Pérez-Montero et al. (2007). Thus, we regard ID-8 as an SFG. We also classify ID-10 as an SFG because the high ionization lines of N IV λ 1487, C IV λ 1548, 1550, and He II λ 1640 are very weak (Stark et al. 2014). Although ID-6 does not show the high ionization line of N V λ 1240, the large values of N IV λ 1483, 1487/N III λ 1750 = 2.3 and C IV λ 1548, 1551/C III λ 1907, 1909 = 6.1 can be produced by a hard ionizing source spectrum. The spectrum of ID-6 may be contaminated by an AGN activity. In summary, we classify ID-8 and ID-10 as SFGs, while ID-6 could possibly be an AGN.

3.2 Reliable Sample

We aim at studying SFGs at $z \sim 2$ with no AGN contamination and no systematic uncertainties. We identify that four out of our eleven galaxies, ID-2, ID-6, ID-7, and ID-8, would have potential problems of AGN and/or systematics. ID-2 has line fluxes of H β , [O III] λ 4959, 5007, H α , and [N II] λ 6584 that are under the potentially large influences of telluric absorption lines (Christensen et al. 2012b). ID-6 has only one Balmer line (H β) that is detected. No Balmer decrement analysis can be applied to ID-6 for dust-extinction correction. Although the SED fitting suggests that ID-6 is free from dust extinction (Fosbury et al. 2003; Villar-Martín et al. 2004), the dust-extinction corrected line fluxes of ID-6 are not as reliable as those of the other galax-

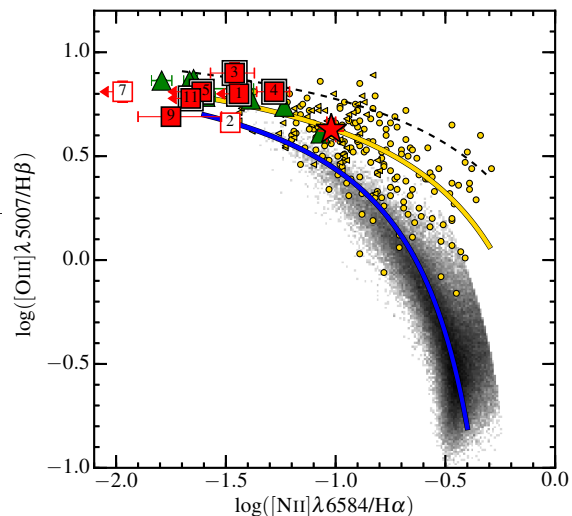


Fig. 3. [O III] 5007/H β vs. [N II] 6584/H α BPT diagram for our $z \sim 2$ galaxies. The red squares denote our galaxies, while the red filled squares are our galaxies in the reliable sample. The numbers written on the red squares are the ID numbers of our galaxies (Table 2–4). In our $z \sim 2$ galaxies, only 8 galaxies are plotted because the spectra of the other 3 galaxies, ID-6, ID-8, and ID-11, do not cover the wavelength of the [N II] line. The yellow circles are the UV-selected galaxies at $z = 2.3$ from KBSS (Steidel et al. 2014). The yellow triangles are the same as the yellow circles, but for the KBSS galaxies with the upper limits of [N II]/H α . The yellow solid line is the best-fit BPT sequence for the KBSS galaxies. The grayscale indicates the distribution of the local SDSS galaxies. The blue solid line is the best-fit sequence of the SDSS galaxies (Kewley & Ellison 2008). The black dashed line represents the maximum theoretical model of star forming galaxies at $z = 2$ (Kewley et al. 2013a). We also plot the S16-stack with the red star, and nine green pea galaxies with the green triangles (Amorín et al. 2012; Jaskot & Oey 2013, see Section 5.1). The $z \sim 2$ galaxies with $EW_0(\text{Ly}\alpha) > 20 \text{ \AA}$ are marked with the large black squares. For our galaxies, the upper limits of [N II]/H α correspond to the 2σ levels.

ies. Moreover, ID-6 may be contaminated by an AGN (Section 3.1). Similarly, ID-7 has a potential uncertainty in the dust-extinction estimates. The emission line of H α is detected in the wavelength with the low instrumental response that may include an unknown systematics. As presented in Section 4, the low values of $12+\log(\text{O}/\text{H})$ and q_{ion} of ID-7 would be produced by the large potential uncertainty of the H α line flux that gives the uncertainty in the $E(B - V)_{\text{neb}}$ estimation. Another uncertainty in the dust extinction correction may exist in ID-8. The measurement of H γ for ID-8 would not be reliable due to the poor atmospheric throughput at the wavelength of H γ . Although we obtain $E(B - V)_{\text{neb}}=0.0$ for ID-8 from the Balmer decrement measurement (Table 4), this value is not consistent with the extinction of $A_v = 1.0$ estimated from the SED fitting (Bayliss et al. 2014). We find that there are no potential problems in the other 7 galaxies (ID-1, ID-3, ID-4, ID-5 ID-9, ID-10, and ID-11) and the S16-stack. We make a subsample of these 7 galaxies and the S16-stack, and refer the subsample as “reliable sample”.

Table 4. Balmer Line Fluxes and the Color Excess

ID	Object	H δ 4101	H γ 4340	H β 4861	H α 6563	$E(B - V)_{\text{neb}}$ (mag)	Notes
(1)	(2)	(3)	(4)	(5)	(6)	(7)	(8)
1	COSMOS 12805	$1.0 \pm 0.3^\dagger$	$2.84 \pm 0.05^\dagger$	$0.01^{+0.43}_{-0.01}$...
2	SMACS 0304	$0.257 \pm 0.005^\dagger$	$0.412 \pm 0.003^\dagger$	1.000 ± 0.002^a	3.604 ± 0.001^a	0.00 ± 0.00	...
3	BX74	1.0^\dagger	$3.46 \pm 0.25^\dagger$	$0.17^{+0.06}_{-0.07}$...
4	BX418	1.0^\dagger	$2.81 \pm 0.2^\dagger$	$0.00^{+0.06}_{-0.00}$...
5	BX660	1.0^\dagger	$2.77 \pm 0.2^\dagger$	$0.00^{+0.03}_{-0.00}$...
6	the Lynx arc	1.0	A
7	Abell 22.3	$1.0 \pm 0.1^\dagger$	$5.03 \pm 0.4^{\text{b}\dagger}$	$0.51^{+0.12}_{-0.10}$	B
8	SGAS 1050	...	0.52 ± 0.02^c	$1.00 \pm 0.01^\dagger$...	0.00 ± 0.00	B
9	CSWA 20	...	0.57 ± 0.05	$1.00 \pm 0.07^\dagger$	$3.32 \pm 0.20^\dagger$	$0.14^{+0.08}_{-0.09}$...
10	MACS 0451	$1.0 \pm 0.1^\dagger$	$2.58 \pm 0.16^\dagger$	$0.00^{+0.04}_{-0.00}$...
11	Abell 860_359	$1.00 \pm 0.03^\dagger$	$2.97 \pm 0.03^\dagger$	0.04 ± 0.03	...
12	S16-stack	$1.00 \pm 0.02^\dagger$	$3.61 \pm 0.02^\dagger$	0.21 ± 0.02	...

(1): ID. (2): Name of the object. (3)–(6): Fluxes of the Balmer lines normalized by H β emission-line fluxes. These Balmer line fluxes are *not* corrected for dust extinction. (7): Color excess derived from the Balmer decrements. (8): “A” denotes a galaxy with no Balmer decrement measurement and $E(B - V)_{\text{neb}}$. “B” indicates a galaxy with potential uncertainties that are originated from the strong sky lines or the low throughputs at the wavelengths of the Balmer lines.

^a Under the influence of telluric absorption lines.

^b Under the influence of the low instrumental response at the wavelength of H α .

^c Under the influences of the poor atmospheric throughput and the moderately strong sky lines.

[†] Balmer lines used for the $E(B - V)_{\text{neb}}$ estimate.

Table 5. Balmer Decrements from the Model

T_e (K)	H α /H β	H γ /H β	H δ /H β
(1)	(2)	(3)	(4)
5000	3.04	0.458	0.251
10000	2.86	0.468	0.259
20000	2.75	0.475	0.264

Under the assumption of the Case B recombination with $n_e = 100 \text{ cm}^{-3}$ (Osterbrock 1989). (1): Electron temperature. (2)–(4): Balmer line ratios.

4 ANALYSIS

In this section, we estimate electron temperatures (T_e), oxygen abundances (O/H), ionization parameters (q_{ion}), and nitrogen to oxygen abundance ratios (N/O) for the eleven galaxies and the S16-stack in our sample. In this paper, we regard these estimates as the average values of the galaxies, because the current telescopes and instruments cannot resolve the H II regions in $z \sim 2$ galaxies. The uncertainties of T_e , O/H, q_{ion} , and N/O are estimated by the Monte Carlo simulations, where the uncertainties in the flux measurements are propagated to the T_e , O/H, q_{ion} , and N/O estimates. We also include the uncertainties of the dust extinction correction. The uncertainties obtained in this way are presented in Table 2.

We construct plane-parallel photoionization models with CLOUDY. We assume solar abundance ratios for all of the elements, except for helium, carbon, and nitrogen. We use forms of Pilyugin et al. (2012a) and Dopita et al. (2006b) for nitrogen and carbon+helium, respectively. Photoionization models are cal-

culated with the gas-phase metallicities of $12 + \log(\text{O}/\text{H}) = (7.54, 7.69, 7.99, 8.17, 8.29, 8.39, 8.59, 8.69)$, the ionization parameters of $\log(q_{\text{ion}} / \text{cm s}^{-1}) = (7.0, 7.2, 7.4, 7.6, 7.8, 8.0, 8.2, 8.4, 8.6, 8.8, 9.0)$, and hydrogen density of $n_{\text{H}} = 250 \text{ cm}^{-3}$ given by Steidel et al. (2014), Shimakawa et al. (2015), and Sanders et al. (2016). Under the assumption that the hydrogen atoms are fully ionized in the H II regions, the hydrogen density of $n_{\text{H}} = 250 \text{ cm}^{-3}$ is justified for our sample, because the median value of $n_e \sim 300 \text{ cm}^{-3}$ are obtained for five galaxies of ID-2–5 and ID-9 that have n_e indicators of [O II] $\lambda\lambda 3727, 3729$ flux measurements (Christensen et al. 2012a; Steidel et al. 2014; James et al. 2014). The incident radiation spectra are generated by stellar synthesis modeling with STARBURST99 (Leitherer et al. 1999, 2010, 2014). In the STARBURST99 models, we adopt instantaneous burst models at zero age with a Kroupa (2001) IMF and lower and upper mass limits of 0.1 and $120 M_{\odot}$, respectively. The stellar atmosphere models of WM-Basic (Pauldrach et al. 2001) and CMFGEN (Hillier & Miller 1998, 1999) are used here. Note that there remains an uncertainty in the selection of stellar atmosphere models, which can affect the calculation results of the CLOUDY models. Stellar metallicities are matched to the gas-phase ones. Our calculations are terminated when the hydrogen ionization fractions reach $\leq 1\%$.

4.1 Electron Temperature

We estimate T_e values of H II regions in our galaxies with the (semi-)forbidden lines, [O III] $\lambda\lambda 1661, 1666$, [O III] $\lambda 4363$, and [O III] $\lambda 5007$. Figure 4 presents the T_e dependence of the two

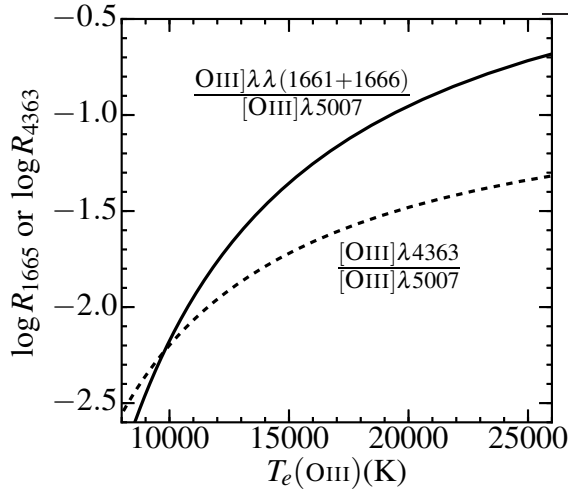


Fig. 4. Flux ratios, R_{1665} (solid line) and R_{4363} (dashed line), as a function of electron temperature $T_e(\text{O III})$. The flux ratios are defined as $R_{1665} = [\text{O III}] \lambda\lambda 1661, 1666 / [\text{O III}] \lambda 5007$ and $R_{4363} = [\text{O III}] \lambda 4363 / [\text{O III}] \lambda 5007$. These R_{1665} and R_{4363} values are obtained by the *nebular.temden* routine of IRAF/STSDAS under the assumption of the low electron density limit.

flux ratios, $R_{1665} \equiv [\text{O III}] \lambda\lambda(1661+1666) / [\text{O III}] \lambda 5007$ (solid line) and $R_{4363} \equiv [\text{O III}] \lambda 4363 / [\text{O III}] \lambda 5007$ (dashed line). From the measurements of R_{1665} and R_{4363} , we obtain T_e values with the *nebular.temden* routine (Shaw & Dufour 1995) in IRAF/STSDAS, assuming the low n_e limit. If n_e is significantly lower than the critical densities, these (semi-)forbidden line fluxes only depend on T_e . The critical densities of $[\text{O III}] \lambda 5007$, $[\text{O III}] \lambda 4363$, and $[\text{O III}] \lambda\lambda 1661, 1666$ are 6.4×10^5 , 2.8×10^7 , and $3.4 \times 10^{10} \text{ cm}^{-3}$, respectively. It is reported that the n_e values of $z = 2-3$ SFGs are clearly low, $\lesssim 10^4 \text{ cm}^{-3}$ based on the estimates with the line ratios of $[\text{O II}] \lambda\lambda 3727/3729$ and $[\text{S II}] \lambda\lambda 6716/6731$ (Shimakawa et al. 2015; Sanders et al. 2016). Thus, the dependence of n_e is negligible in our T_e estimates. Because one of the $[\text{O III}]$ doublet lines, $[\text{O III}] \lambda 1661$, is not detected in our 3 galaxies (ID-9, ID-10, and ID-11), we assume $[\text{O III}] \lambda\lambda 1666/1661 = 2.46$ for these 3 galaxies. It should be noted that the ratio of $[\text{O III}] \lambda\lambda 1666/1661 = 2.46$ marginally depends either on T_e or n_e . We confirm the marginal dependence on T_e or n_e with our CLOUDY model calculations, suggesting that a change of the $[\text{O III}]$ ratio is less than 0.01 dex in the parameter ranges of $\log(q_{\text{ion}}/\text{cm s}^{-1}) = 7.5-9.0$ and $12 + \log(\text{O}/\text{H}) = 7.54-8.69$. In this way, we obtain T_e values of our galaxies, which are typically $\sim 10,000-20,000 \text{ K}$. Table 2 and Figure 5 summarize the T_e values of our galaxies.

Note that ID-7 and ID-10 have high T_e values of $\sim 30,000 \text{ K}$ and $\sim 22,000 \text{ K}$, respectively. The unrealistically high T_e value of ID-7 is due to the large $\text{H}\alpha/\text{H}\beta$ ratio of 5.03, which is probably biased by the systematic error of the telluric absorption correction for the $\text{H}\alpha$ line flux estimate. Thus we do not include ID-7 in the reliable sample. In contrast with ID-7, we find no

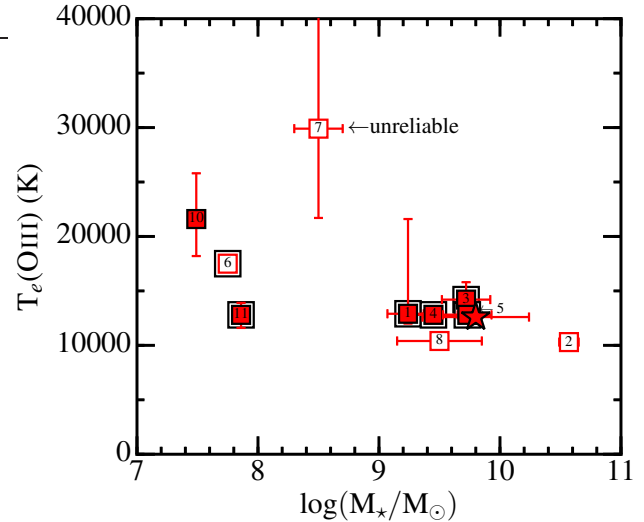


Fig. 5. Electron temperature measurements of our $z \sim 2$ galaxies as a function of stellar mass. The red squares denote our galaxies, while the red filled squares are our galaxies in the reliable sample. The numbers written on the red squares are the ID numbers of our galaxies (Tables 2–4). The data point of ID-9 is not shown because an M_* measurement of ID-9 is not available. We also plot the S16-stack with the red star. The $z \sim 2$ galaxies with $\text{EW}_0(\text{Ly}\alpha) > 20 \text{ \AA}$ are marked with the large black squares.

possible systematics in the ID-10 flux measurements. However, it is unclear whether we can apply *nebular.temden* over 20,000 K because *nebular.temden* uses the $[\text{O III}]$ collisional strengths that are confirmed to be valid only below 20,000 K (Seaton 1975). Thus we compare the T_e values that are obtained with the *nebular.temden* routine and the CLOUDY model. CLOUDY uses the $[\text{O III}]$ collisional strengths that are valid from $\sim 1,000 \text{ K}$ to $\sim 100,000 \text{ K}$ (Dere et al. 1997). We find that the T_e differences between *nebular.temden* and CLOUDY are less than 1 per cent around 22,000 K.² Thus we think that the T_e value of ID-10 is reliably estimated.

In addition, we find that the T_e value of ID-10 ($\sim 22,000 \text{ K}$) falls in the temperature range of the existing H II regions (Izotov et al. 2012). This indicates that the T_e value of ID-10 ($\sim 22,000 \text{ K}$) is realistic.

4.2 Oxygen Abundance

We estimate oxygen abundances with the direct T_e methods. Here, we adopt

$$\frac{\text{O}}{\text{H}} = \frac{\text{O}^+ + \text{O}^{2+}}{\text{H}^+} \quad (3)$$

for H II regions of SFGs. We ignore oxygen ions of O^{3+} because the ionization potential of O^{3+} is 54.9 eV, too high for the stellar radiation to produce O^{3+} . We estimate ionic oxygen abundances of O^+ and O^{2+} with the relations (Izotov et al.

² We also confirm that the T_e differences between *nebular.temden* and CLOUDY are less than 1 per cent in the range of 10,000–22,000 K.

2006),

$$12 + \log\left(\frac{\text{O}^+}{\text{H}^+}\right) = \log\left(\frac{[\text{O II}] \lambda 3727}{\text{H}\beta}\right) + 5.961 + \frac{1.676}{t_2} - 0.40 \log t_2 - 0.034 t_2 \quad (4)$$

$$12 + \log\left(\frac{\text{O}^{2+}}{\text{H}^+}\right) = \log\left(\frac{[\text{O III}] \lambda \lambda 4959 + 5007}{\text{H}\beta}\right) + 6.200 + \frac{1.251}{t_3} - 0.55 \log t_3 - 0.014 t_3, \quad (5)$$

where we omit the term of n_e that is negligibly small. In Equations (4) and (5), we define $t_2 = 10^{-4} T_e(\text{O II})$ and $t_3 = 10^{-4} T_e(\text{O III})$, where $T_e(\text{O II})$ and $T_e(\text{O III})$ are electron temperatures measured with $[\text{O II}]$ and $[\text{O III}]$, respectively. Because auroral lines of $[\text{O II}]$ ($[\text{O II}] \lambda \lambda 7320, 7330$) are not observed in our galaxies, we assume

$$t_2 = 0.7 t_3 + 0.3 \quad (6)$$

(Campbell et al. 1986; Garnett 1992). Note that our conclusions of the oxygen abundance little depend on the assumption of t_2 . This is because our galaxies generally have high values of $\log(\text{O}^{2+}/\text{O}^+) \sim 0.8\text{--}1.0$ and the contribution of O^{2+}/H^+ to the oxygen abundance estimate is much larger than the one of O^+/H^+ . In fact, if we change $T_e(\text{O II})$ by ± 2000 K, the oxygen abundance $12 + \log(\text{O}/\text{H})$ differs only by < 0.04 dex. By these calculations, we obtain $12 + \log(\text{O}/\text{H}) = 7.3\text{--}8.4$ for our galaxies. Our $12 + \log(\text{O}/\text{H})$ estimates are summarized in Table 2.

4.3 Ionization Parameter

We estimate the ionization parameters q_{ion} with O_{32} using the grids of the photoionization models (Kewley & Dopita 2002). Here, q_{ion} is defined as

$$q_{\text{ion}} = \frac{S_{\text{H}^0}}{n_{\text{H}}}, \quad (7)$$

where n_{H} is the density of hydrogen and S_{H^0} is the flux of ionizing photons at the inner surface of the plane-parallel slab. Although an O_{32} measurement is sensitive to both q_{ion} and $12 + \log(\text{O}/\text{H})$, we have the estimate of $12 + \log(\text{O}/\text{H})$ given by the direct T_e methods (Section 4.2). Thus, our q_{ion} measurements do not include systematic uncertainties originated from the degeneracy with $12 + \log(\text{O}/\text{H})$ estimates that is found in the strong line method results. Table 2 summarizes the q_{ion} estimates. Seven out of our eleven galaxies have the values of $\log(q_{\text{ion}}/\text{cm s}^{-1}) = 7.7\text{--}8.6$, while the other four galaxies have the lower limits at $\log(q_{\text{ion}}/\text{cm s}^{-1}) = 7.8\text{--}8.6$. The S16-stack have $\log(q_{\text{ion}}/\text{cm s}^{-1}) = 7.70$.

4.4 Nitrogen-to-Oxygen Abundance Ratio

We calculate N/O values with the line fluxes of $[\text{N II}] \lambda 6584$ and $[\text{N III}] \lambda 1750$ by the direct T_e methods.

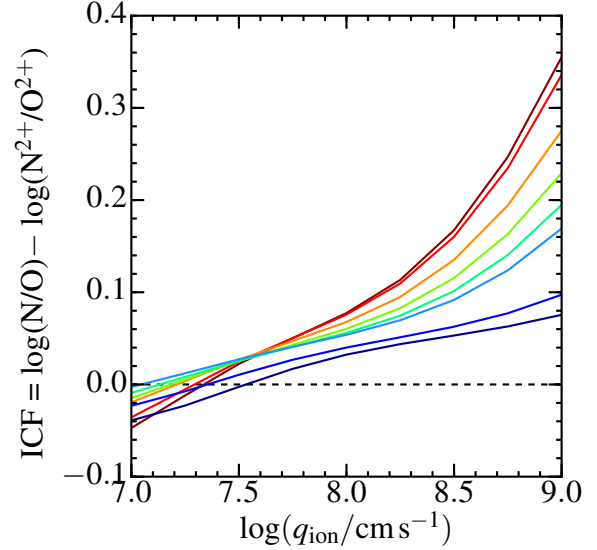


Fig. 6. Ionization correction factors (ICFs) obtained from our CLOUDY models. The solid lines are ICFs with the color codes defined by $12 + \log(\text{O}/\text{H})$. The $12 + \log(\text{O}/\text{H})$ values are 7.54, 7.69, 7.99, 8.17, 8.29, 8.39, 8.59 and 8.69, which correspond to the colors from dark red to dark blue. The black dashed line indicates $\text{ICF}=0$.

For the six $z \sim 2$ galaxies (ID-2, ID-3, ID-4, ID-5, ID-7, and ID-9) and the S16-stack with $[\text{N II}] \lambda 6584$ and $[\text{O II}] \lambda 3727$ lines, we calculate

$$\log\left(\frac{\text{N}^+}{\text{O}^+}\right) = \log\left(\frac{[\text{N II}] \lambda 6584}{[\text{O II}] \lambda 3727}\right) + 0.400 - \frac{0.726}{t_2} - 0.02 \log t_2 + 0.007 t_2, \quad (8)$$

which is given by Izotov et al. (2006) under the assumption of $[\text{N II}] \lambda \lambda 6584/6548 = 2.95$. We estimate N/O with

$$\frac{\text{N}}{\text{O}} \simeq \frac{\text{N}^+}{\text{O}^+} \quad (9)$$

(Peimbert 1967). Note that the ionic ratio of N^+/O^+ is a good indicator of N/O because ionization potentials of neutral oxygen and nitrogen are almost the same. Our CLOUDY models confirm that the uncertainties of the N/O estimates from Equations (8) and (9) are less than 0.04 dex and 0.05 dex, respectively, in the parameter ranges of $\log(q_{\text{ion}}/\text{cm s}^{-1}) = 7.0\text{--}9.0$ and $12 + \log(\text{O}/\text{H}) = 7.54\text{--}8.69$ (see also Garnett 1990).

For the other 5 galaxies to which we cannot apply Equation (8), we use the fluxes of $[\text{N III}] \lambda 1750$ and $[\text{O III}] \lambda \lambda 1661 + 1666$ to calculate

$$\log\left(\frac{\text{N}^{2+}}{\text{O}^{2+}}\right) = \log\left(\frac{[\text{N III}] \lambda 1750}{[\text{O III}] \lambda \lambda 1661 + 1666}\right) - 0.674 - \frac{0.187}{t_3} \quad (10)$$

(Garnett et al. 1995). We then estimate the N/O from the $\text{N}^{2+}/\text{O}^{2+}$ ratio with the ionization correction factor (ICF),

$$\log\left(\frac{N}{O}\right) = \log\left(\frac{N^{2+}}{O^{2+}}\right) + \text{ICF}. \quad (11)$$

We obtain the ICF values from our CLOUDY models, which are shown in Figure 6. Although the q_{ion} dependence of ICF is not very large (< 0.2 dex in the parameter ranges of $\log(q_{\text{ion}}/\text{cm s}^{-1}) = 7.5\text{--}8.6$ and $12+\log(\text{O}/\text{H}) = 7.54\text{--}8.69$ in Figure 6), we use the correction factors of ICF.

By these calculations, we find that six out of our eleven galaxies have values of $\log(N/O)_{T_e} = (-1.6)\text{--}(-1.0)$, while the other five galaxies have upper limits ranging from -1.7 to -1.3 . We obtain the value of $\log(N/O)_{T_e} = -1.21$ for the S16-stack. Table 2 presents the N/O values of our sample.

Note that it is worth comparing the N/O estimates from N^+/O^+ (eqs. 8 and 9) and N^{2+}/O^{2+} (eqs. 10 and 11) ratios of an object for the consistency check. However, we cannot make this comparison, because there are no objects with both N^+/O^+ and N^{2+}/O^{2+} measurements (or constraints). Although ID-1 and 10 have the N/O upper limits estimated from N^{2+}/O^{2+} ratios, these two objects have no constraints on N/O obtained by N^+/O^+ ratios, due to the given upper limits of both [O II] $\lambda 3727$ and [N II] $\lambda 6584$ fluxes.

5 RESULTS AND DISCUSSION

In this section, we present the results of our analysis given in Section 4, and compare them with average measurements from stacks of the 208,529 SDSS galaxies given by Andrews & Martini (2013) whose physical properties are determined by the direct T_e methods. We refer to these SDSS galaxy stacks as ‘‘local stacks’’. Andrews & Martini (2013) made two kinds of the local stacks, M_* and $M_*\text{--SFR}$ stacks. The M_* stacks are the stacked spectra binned in M_* , while the $M_*\text{--SFR}$ stacks are those binned in M_* and SFR. The SFR and M_* values are taken from the MPA-JHU value-added catalog³ (Kauffmann et al. 2003; Brinchmann et al. 2004; Salim et al. 2007). The M_* values are adjusted to the Chabrier IMF for comparison. We use N/O values determined by Andrews & Martini (2013), whereas we estimate q_{ion} of the local stacks in the same manner as Section 4.3.

In Figure 7, we plot $\log(N/O)$ as a function of $\log(M_*/M_\odot)$ for the $z \sim 0$ SDSS galaxies. Figure 7 shows not only the $\log(N/O)$ estimates from the direct T_e methods, but also those from the strong line methods calculated with [N II] $\lambda 6584$ /[O II] $\lambda 3727$ (\equiv N2O2) and [N II] $\lambda 6584$ /[S II] $\lambda\lambda(6717+6731)$ (\equiv N2S2) by the procedures of Pérez-Montero & Contini (2009). This plot shows that the strong line method gives a systematic bias that elevates the $\log(N/O)$ estimates. This systematic bias may be made by the incorrect calibration due to the missing low T_e systems. Thus, the direct T_e methods

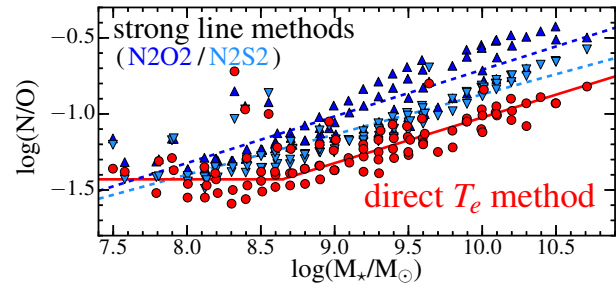


Fig. 7. $\log(N/O)$ as a function of $\log(M_*/M_\odot)$ for the $z \sim 0$ galaxies used in our comparisons. The red circles indicate the SDSS galaxies whose $\log(N/O)$ is derived with the direct T_e methods (Andrews & Martini 2013). The blue triangles and cyan inverted triangles are the same as the red circles, but with $\log(N/O)$ values estimated by the strong line methods of N2O2 and N2S2, respectively, calibrated by Pérez-Montero & Contini (2009) (see text). The red-solid and blue-dashed lines denote the linear functions representing the averages of the red circles and blue triangles, respectively, with the statistical weights of the galaxy numbers. This plot demonstrates that the strong line method gives a systematic bias that increases the $\log(N/O)$ estimates, and that the direct T_e methods are needed for the fair comparisons of the $z \sim 0$ and $z \sim 2$ galaxies.

are needed for the fair comparisons of the $z \sim 0$ and $z \sim 2$ galaxies. We use $\log(N/O)$ estimates from the direct T_e methods both for the $z \sim 0$ and $z \sim 2$ galaxies.

As explained in Section 3, we assume the dust extinction curve of Cardelli et al. (1989) in this paper. However, the assumption of the dust extinction curve might change the results of this paper. Thus we also calculate the values of T_e , O/H, q_{ion} , and N/O under the assumption of the dust extinction curve of Calzetti et al. (2000), and check whether the results in this section change. We have confirmed that the results in this section do not change by the assumption of the dust extinction curve. This is because our galaxies have low $E(B - V)_{\text{neb}}$ values (Table 4).

5.1 Mass–Metallicity–SFR Relation

The top panel of Figure 8 shows the mass–metallicity ($M_*\text{--O}/\text{H}$) relation for our $z \sim 2$ galaxies and the local $M_*\text{--SFR}$ stacks. For comparison, we also plot nine green pea galaxies (GPs) with the triangles. These nine GPs are composed of three normal GPs (Amorín et al. 2012) and six extreme GPs with high O_{32} values (Jaskot & Oey 2013). We find that most of our $z \sim 2$ galaxies, the S16-stack, and the nine GPs have $12+\log(\text{O}/\text{H})$ values comparable with those of the local stacks for given M_* and SFR values.

The bottom panel of Figure 8 compares our $z \sim 2$ galaxies, the S16-stack, the local stacks, and GPs in the mass–metallicity–SFR ($M_*\text{--O}/\text{H}\text{--SFR}$) relation. Here the parameter $\mu_{0.66}$ is defined by

$$\mu_{0.66} = \log(M_*) - 0.66 \log(\text{SFR}), \quad (12)$$

³ <http://www.mpa.mpa-garching.mpg.de/SDSS/DR7/>

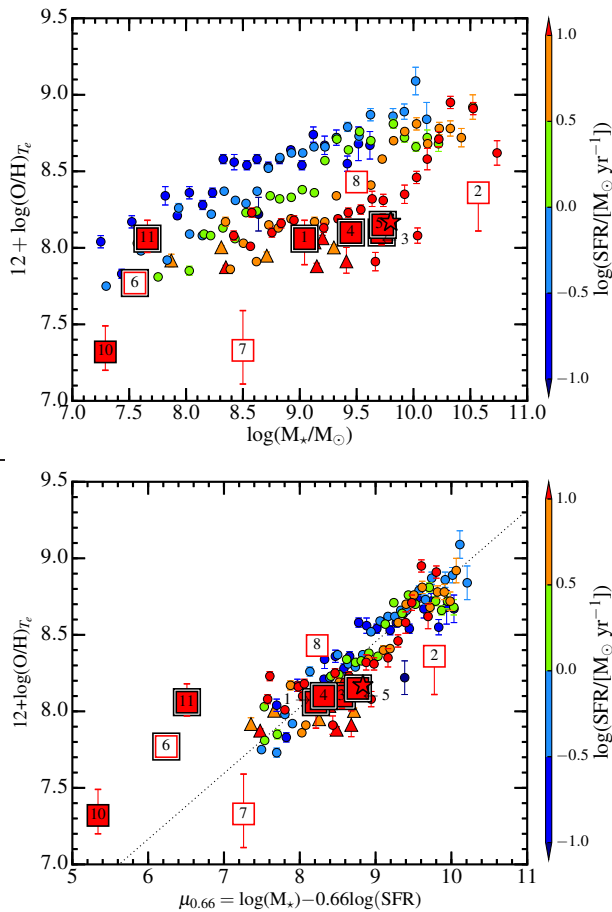


Fig. 8. M_* vs. $12+\log(\text{O}/\text{H})_{T_e}$ (top panel) and $\mu_{0.66}$ vs. $12+\log(\text{O}/\text{H})_{T_e}$ (bottom panel) diagrams with our galaxies and the local M_* –SFR stacks of Andrews & Martini (2013). The red squares denote our $z \sim 2$ galaxies, while the red filled squares are our $z \sim 2$ galaxies in the reliable sample. The numbers written on the red squares are the ID numbers of our galaxies (Table 4). The star mark represents the S16-stack. The circles indicate the local M_* –SFR stacks. The triangles denote the GPs (Amorín et al. 2012; Jaskot & Oey 2013) whose M_* values are taken from Izotov et al. (2011) and Overzier et al. (2009). All of the symbols, the squares, star, circles, and triangles are color-coded by SFRs defined with the color bars at the right sides of the panels. The $z \sim 2$ galaxies with $\text{EW}_0(\text{Ly}\alpha) > 20 \text{ \AA}$ are marked with the large black squares. In the bottom panel, the black dotted line represents the linear fit to the local M_* –SFR stacks (Andrews & Martini 2013). The data point of ID-9 is not shown because a M_* measurement of ID-9 is not available.

which is introduced by Mannucci et al. (2010). The coefficient of 0.66 is obtained by Andrews & Martini (2013) to minimize the scatter of the local M_* –SFR stacks. Seven out of the eleven $z \sim 2$ galaxies, the S16-stack, and the nine GPs have $12+\log(\text{O}/\text{H})$ values comparable with those of the local stacks at fixed $\mu_{0.66}$. The $\mu_{0.66}$ values of ID-6, ID-10, and ID-11 range in $5 \lesssim \mu_{0.66} \lesssim 7$, where we find no counterparts in the local M_* –SFR stacks. Thus, we cannot compare these three galaxies with the local M_* –SFR stacks. It should be noted that these three galaxies are located above the extrapolation of the best fit line of the local stacks.

5.2 N/O Abundance Ratio

5.2.1 Overall Comparisons

Figure 9 presents $\log(\text{N}/\text{O})_{T_e}$ values of $z \sim 2$ galaxies as functions of $\log(M_*/M_{\odot})$ and $12+\log(\text{O}/\text{H})_{T_e}$ in the top and bottom panels, respectively. We find that our galaxies range in $\log(\text{N}/\text{O})_{T_e} \lesssim -1.0$, $12+\log(\text{O}/\text{H})=7.3\text{--}8.5$, and $\log(M_*/M_{\odot}) = 7.5\text{--}10.5$. We also show the S16-stack (star mark), the local stacks (circles), and the nine GPs (triangles). The best-fit results of the local M_* stacks are indicated with the black lines in Figure 9. Although the black lines do not appear at the center of the distribution of the circles in Figure 9, the black lines represent the average of the local stacks that is weighted with the numbers of galaxies making the local stacks. We refer to these black lines as a “local sequence”. Although there are many N/O–O/H relations obtained in various objects (e.g., Groves et al. 2004; Pérez-Montero & Contini 2009; Pilyugin et al. 2012b), we only exhibit the local stacks made by Andrews & Martini (2013) for a comparison. This is because our $z \sim 2$ galaxies should be compared with typical $z \sim 0$ SFGs whose N/O values are also based on the direct T_e method. Because the local stacks are selected homogeneously, the local stacks are representative of typical $z \sim 0$ SFGs. Moreover, the physical properties of the local stacks are determined by the direct T_e method. Below we make two comparisons with the local sequence.

First, we compare our $z \sim 2$ galaxies with the local sequence on an *individual* basis. In the top panel of Figure 9, we present the N/O– M_* plot for $z \sim 2$ galaxies whose N/O values are derived by the direct T_e method. Most of our $z \sim 2$ galaxies have $\log(\text{N}/\text{O})_{T_e}$ values comparable with or lower than those of the local sequence. Some objects have N/O values smaller than the local sequence beyond the errors. This trend supports the previous observational results for $z \sim 2$ galaxies based on the strong line method (Kashino et al. 2017; Strom et al. 2016). Masters et al. (2016) suggest that N/O decrements in the N/O– M_* relation can be explained by the $z \sim 2$ stellar population younger than the $z \sim 0$ stellar population for a given M_* . In the bottom panel of Figure 9, ID-3, ID-4, ID-6, the S16-stack, and most of the GPs have $\log(\text{N}/\text{O})_{T_e}$ values about 0.2–0.4 dex larger than that of the local sequence ($\log(\text{N}/\text{O})_{T_e} = -1.43$) significantly beyond the measurement errors. These three galaxies and the S16-stack are N/O-excess galaxies, where the word of N/O excess is hereafter used for objects that fall above the local sequence of the N/O–O/H relation. The other eight $z \sim 2$ galaxies have N/O values comparable to the local sequence.

Second, we compare the *average* of our $z \sim 2$ galaxies with the local sequence in the N/O–O/H relation. We calculate the average value of N/O, using all of the eleven $z \sim 2$ galaxies and the S16-stack with the weights of galaxy numbers and measurement uncertainties. Because 5 out of our eleven $z \sim 2$ galaxies have upper limits on N/O, we only derive an upper limit of the

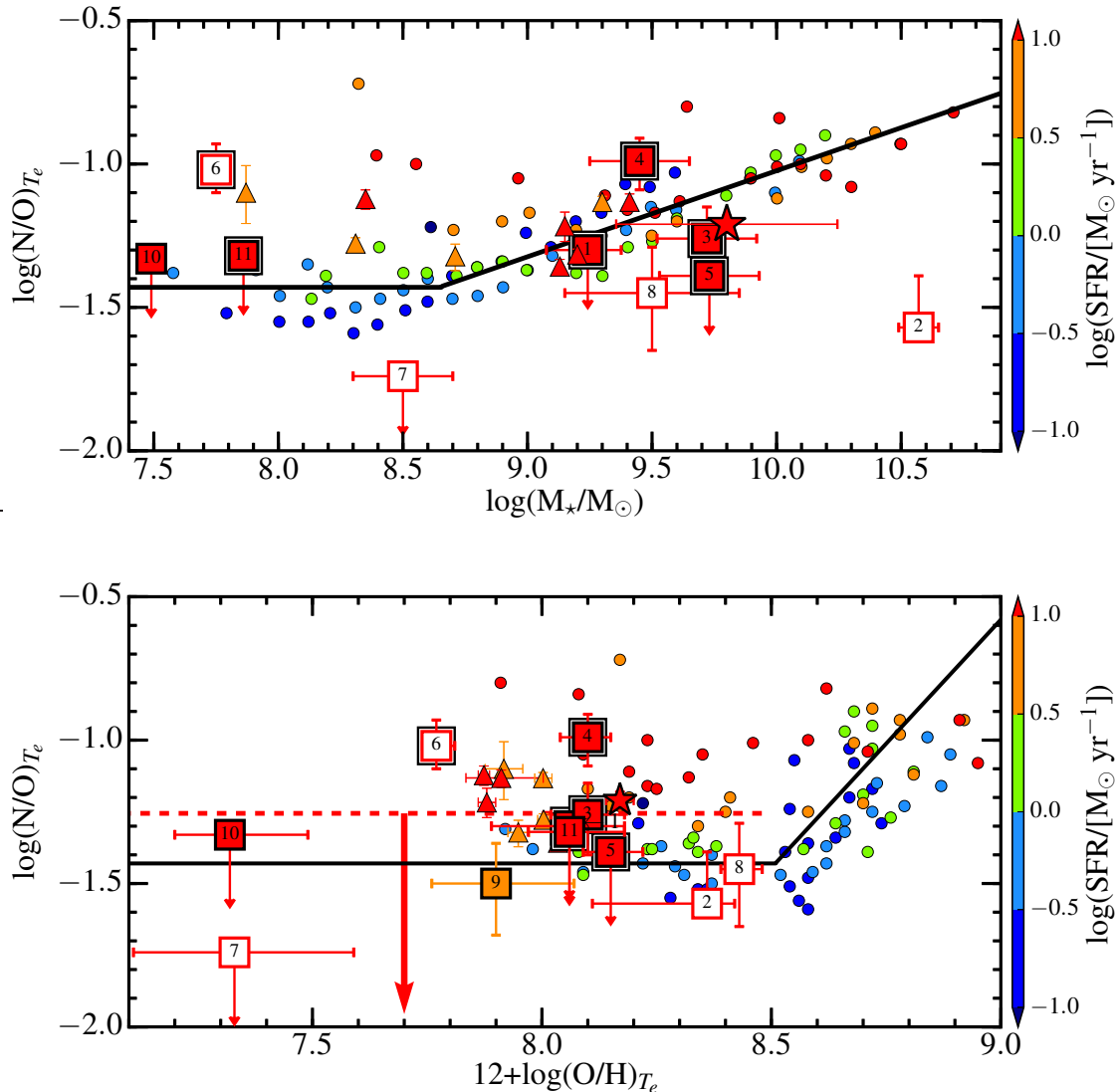


Fig. 9. Diagrams of $\log(\text{N/O})_{T_e}$ vs. $\log(M_*/M_{\odot})$ (top panel) and $\log(\text{N/O})_{T_e}$ vs. $12 + \log(\text{O/H})_{T_e}$ (bottom panel). The squares represent our $z \sim 2$ galaxies, while the filled squares are our $z \sim 2$ galaxies in the reliable sample. The star mark indicates the S16-stack. The circles show the local M_* -SFR stacks of Andrews & Martini (2013). The triangles denote the GPs (Amorin et al. 2012; Jaskot & Oey 2013). All of the symbols, squares, star, circles, and triangles, have the color coding of SFR whose definition is the same as Figure 8. The $z \sim 2$ galaxies with $\text{EW}_0(\text{Ly}\alpha) > 20 \text{ \AA}$ are marked with the large black squares. The black solid lines represent the local sequence of Andrews & Martini (2013). Although the black lines do not appear at the center of the distribution of the circles, the black lines represent the average values of the local stacks that are weighted by the numbers of galaxies (see text). In the bottom panel, the red dashed line represents the upper limit of the average N/O value given by our $z \sim 2$ galaxies ($\log(\text{N/O})_{T_e} = -1.26$). In the top panel, the data point of ID-9 is not shown because M_* of ID-9 is not available. All of the upper limits of $\log(\text{N/O})_{T_e}$ indicated with the arrows correspond to the 2σ levels.

N/O average. We thus obtain the stringent upper limit on the average N/O value. The obtained average upper limit of our eleven galaxies and the S16-stack is $\log(\text{N/O})_{T_e} < -1.26$. We show the average upper limit with the red dashed line in the bottom panel of Figure 9. The average upper limit is higher than the local sequence by 0.17 dex in N/O, suggesting that the N/O ratios do not increase from $z \sim 0$ to $z \sim 2$ by more than 0.17 dex on average for a given O/H.

From these comparisons above, we confirm that most of our galaxies have N/O values comparable with (or lower than) that of the local sequence in the N/O– M_* relation, although some of the $z \sim 2$ galaxies show the significant N/O excess above the local sequence in the N/O–O/H relation. In Section 1, we have discussed the two possible physical origins of the N/O excess: the pristine gas inflow and the nitrogen enrichment by the enhanced WR population. The pristine gas inflow is likely to cause O/H decrements while N/O and M_* values change very little (Andrews & Martini 2013), which means that an N/O excess appears only in the N/O–O/H relation. If the enhanced WR population enriches ISM with nitrogen, N/O values are likely to increase both in the N/O– M_* and N/O–O/H relation at $z \sim 2$. Thus, our results support the pristine-gas-inflow scenario rather than the WR-star scenario. In addition, we confirm above that an N/O average does not increase very largely toward $z \sim 2$ in the N/O–O/H relations for our sample. This may be primarily because our $z \sim 2$ galaxies consist of relatively low- M_* galaxies whose N/O values are intrinsically smaller than the massive ones. Additionally, N/O decrements in the N/O– M_* relation towards $z \sim 2$ may also contribute to the low N/O value on average.

5.2.2 Comparisons of the Galaxies in the Same Ranges of SFR and M_*

Figure 9 shows that most of the local stacks with high SFRs (red circles) have large N/O ratios of $\log(\text{N/O})_{T_e} = -1.2$ to -0.8 . This is the dependence of N/O ratio on SFR that is claimed by Andrews & Martini (2013). Similarly, the top panel of Figure 9 exhibits a clear dependence of N/O ratio on M_* for the local stacks. Because N/O ratios of local galaxies correlate with SFR and M_* , one needs to compare N/O ratios of local and $z \sim 2$ galaxies in the same ranges of SFR and M_* values.

We find that there is an overlap of the $z \sim 2$ and local galaxies in the parameter ranges of $\log(\text{SFR}/M_\odot \text{ yr}^{-1}) > 1.0$ and $9.0 < \log(M_*/M_\odot) < 10.0$. We choose galaxies in these ranges from our $z \sim 2$ galaxies and the local M_* –SFR stacks. These are galaxies from our reliable sample (ID-1, ID-3, ID-4, and ID-5), the S16-stack, and six local M_* –SFR stacks. The six local M_* –SFR stacks are made of 206 SDSS galaxies in total. We refer to these six local M_* –SFR stacks as low-mass and high-SFR stacks (LMHSs).

Figure 10 presents $\log(\text{N/O})_{T_e}$ as a function of

$12+\log(\text{O/H})_{T_e}$ for ID-1, ID-3, ID-4, ID-5, and the six LMHSs. Figure 10 also shows four out of the nine GPs that fall in the ranges of $\log(\text{SFR}/M_\odot \text{ yr}^{-1}) > 1.0$ and $9.0 < \log(M_*/M_\odot) < 10.0$. The $\log(\text{N/O})_{T_e}$ values of ID-3 and ID-4 are significantly higher than the local sequence by ~ 0.2 – 0.4 dex, but ID-1 and ID-5 have $\log(\text{N/O})_{T_e}$ upper limits comparable with the local sequence. The $\log(\text{N/O})_{T_e}$ average of our sample galaxies is comparable with or lower than those of GPs and LMHSs.

5.3 Ionization Parameter

Figure 11 presents the q_{ion} values of our $z \sim 2$ galaxies, the S16-stack, the local stacks, and the nine GPs as a function of $12+\log(\text{O/H})$. The local stacks indicate the tight anti-correlation between $12+\log(\text{O/H})$ and q_{ion} that are measured by the direct T_e method. This anti-correlation has been reported by Nakajima & Ouchi (2014) and Onodera et al. (2016), who estimate the O/H and q_{ion} values based on the strong line methods. The black line in Figure 11 indicates the average of the local stacks that is the best-fit linear function for the local M_* stacks (open circle) in the range of $\log(q_{\text{ion}}) > 7.4$. The best-fit linear function is

$$\log(q_{\text{ion}}) = -0.68(12 + \log(\text{O/H})_{T_e}) + 13.38. \quad (13)$$

Six out of the nine GPs show q_{ion} values higher than that of the local-stack best-fit function, although GPs are parts of $z \sim 0$ galaxies.

For our sample, seven out of our eleven $z \sim 2$ galaxies (ID-2, ID-3, ID-4, ID-5, ID-6, ID-8, and ID-11) have q_{ion} values falling above the local-stack best-fit function, which are hereafter referred to as q_{ion} excesses. These q_{ion} values of the seven $z \sim 2$ galaxies are similar to those of the GPs with q_{ion} excesses. This result does not change if we compare our reliable-sample galaxies with the GPs. Because we find no q_{ion} dependence on SFR in Figure 11, the high q_{ion} values may not be attributed to high SFRs. It should be noted that the q_{ion} excess can be mimicked by the harder spectrum of ionizing radiation (see Section 1) or the density-bounded H II regions (Nakajima & Ouchi 2014).

In the reliable sample, ID-1, ID-3, ID-4, ID-5, ID-11, and the S16-stack have $\text{EW}_0(\text{Ly}\alpha)$ estimates (Table 2), because Ly α lines are covered in their spectra. The five galaxies of ID-1, ID-3, ID-4, ID-5, and ID-11 have $\text{EW}_0(\text{Ly}\alpha)$ values of 30–160 Å, which are classified as LAEs (defined by $\text{EW}_0(\text{Ly}\alpha) > 20$ Å). In contrast, the S16-stack has a low $\text{EW}_0(\text{Ly}\alpha)$ value of ~ 4 Å. This low $\text{EW}_0(\text{Ly}\alpha)$ value is explained by the fact that the S16-stack is composed of UV-continuum bright galaxies. In Figure 12, we find that the majority of the five LAEs show significant q_{ion} excesses, while the S16-stack has no q_{ion} excess. This result suggests the possibility that there is a positive correlation between q_{ion} and $\text{EW}_0(\text{Ly}\alpha)$, and support the claim of Nakajima

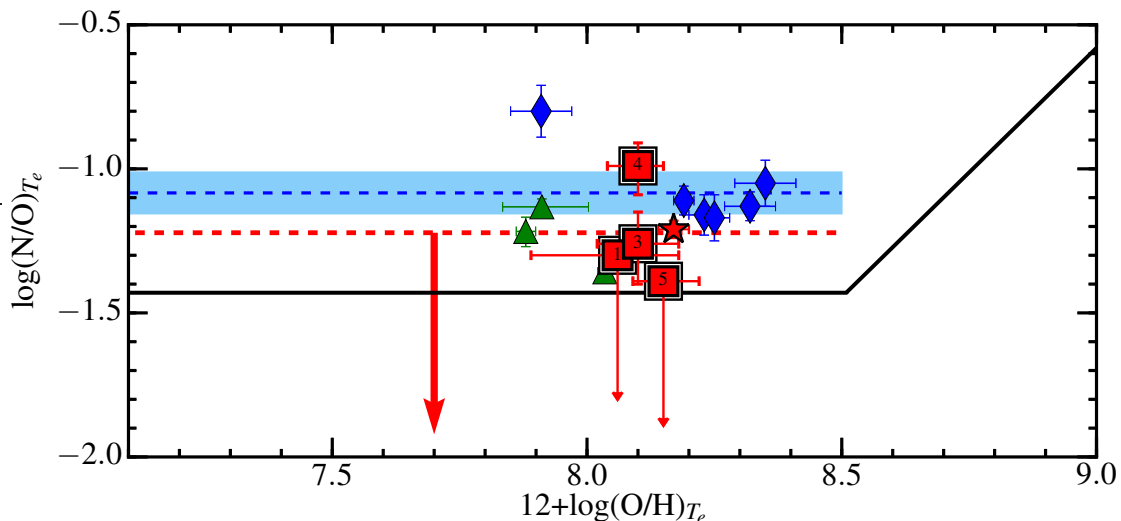


Fig. 10. Same as the bottom panel of Figure 9, but for the galaxies in the parameter ranges of $\log(\text{SFR}/M_{\odot} \text{ yr}^{-1}) > 1.0$ and $9.0 < \log(M_{*}/M_{\odot}) < 10.0$. The blue diamonds and the green triangles indicate the LMHSs (Section 5.2.2) and the GPs (Amorín et al. 2012; Jaskot & Oey 2013), respectively. The red dashed line indicates the upper limit of averaged N/O value that is derived from ID-1, ID-3, ID-4, ID-5, and the S-16 stack. The blue dashed line denotes $\log(\text{N/O})_{T_e} = -1.08$, which is the average of LMHSs with the weight of the number of galaxies, and the blue shaded region represents the 1σ range (± 0.07 dex) for the determination of the blue dashed line.

& Ouchi (2014). Recently, Trainor et al. (2016) also report that Lyman break galaxies (LBGs) with high $\text{EW}_0(\text{Ly}\alpha)$ values show high O_{32} values, indicative of the positive correlation between q_{ion} and $\text{EW}_0(\text{Ly}\alpha)$.

5.4 Physical Origins of the BPT Diagram Offset

In this section, we discuss the positions of the galaxies on the BPT diagram. Figure 13 presents the BPT diagram, which is the same as Figure 3, but for five galaxies (ID-1, 3, 4, 5, and 11) selected from our reliable sample. Similarly, S16-stack is also presented. These five galaxies and the S16-stack have very similar oxygen abundances, which fall in $12+\log(\text{O}/\text{H}) = 8.10 \pm 0.15$. Two out of the five galaxies (ID-3 and ID-4) and the S16-stack significantly exhibit the BPT offsets, while the other three galaxies, ID-1, ID-5 and ID-11, have signatures of possible BPT offsets with $[\text{N II}]/\text{H}\alpha$ upper limits. We also plot the five GPs and the three LMHSs⁴ that have O/H values of $12+\log(\text{O}/\text{H}) = 8.10 \pm 0.15$. In Figure 13, we present the reference galaxy (open circle), which is an average local galaxy with $12+\log(\text{O}/\text{H}) = 8.10$ that shows neither N/O nor q_{ion} excess. More precisely, the reference galaxy is the average of four local stacks (a total of 46 local galaxies) with a metallicity of $12+\log(\text{O}/\text{H}) = 8.10 \pm 0.05$ and no N/O+ q_{ion} excesses. The reference galaxy has N2 and O3 values comparable with the best-fit sequence of the SDSS galaxies (Kewley & Ellison 2008) within the error bar.

In Figure 13, we find that the $z \sim 2$ galaxies and the GPs

⁴ The three LMHSs are 24, 18, and 4 individual galaxy stacks, and composed of a total of 46 (=24+18+4) individual galaxies.

are located very close on the BPT diagram, which is consistent with previous studies (e.g. Steidel et al. 2014). Because the locations on the BPT diagram are degenerated with N/O-excess galaxies and q_{ion} -excess galaxies at different O/H values, no previous study has clearly identified the physical origin of the BPT offsets of $z \sim 2$ galaxies. Our simultaneous measurements of N/O, O/H, and q_{ion} values without systematic uncertainties can break the degeneracy between O/H, N/O, and q_{ion} excesses (Sections 5.2 and 5.3).

From the results in Sections 5.2 and 5.3, the galaxies with $12+\log(\text{O}/\text{H}) = 8.10 \pm 0.15$ are classified into four groups based on the N/O and/or q_{ion} excesses as shown below:

- 0) Galaxies with *neither* N/O nor q_{ion} excess.
- 1) Galaxies with an N/O excess and *no* q_{ion} excess.
- 2) Galaxies with a q_{ion} excess and *no* N/O excess.
- 3) Galaxies with both N/O and q_{ion} excesses.

The classifications of the $z \sim 2$ galaxies, S16-stack, GPs, and LMHSs are summarized in Table 6.

In Figure 13, the galaxies classified into 1), 2), and 3) are surrounded by the cyan, light green, and magenta circles on the BPT diagram, respectively. We find these three groups of galaxies are located separately on the BPT diagram regardless of the redshift. We argue that the BPT offsets are caused by the N/O and q_{ion} excesses while the amounts of the contributions of N/O and q_{ion} are different from galaxy to galaxy.

We construct CLOUDY photoionization models to confirm the relation between the physical properties and the loci on the BPT diagram. Assuming $12+\log(\text{O}/\text{H}) = 8.10$, we calculate the

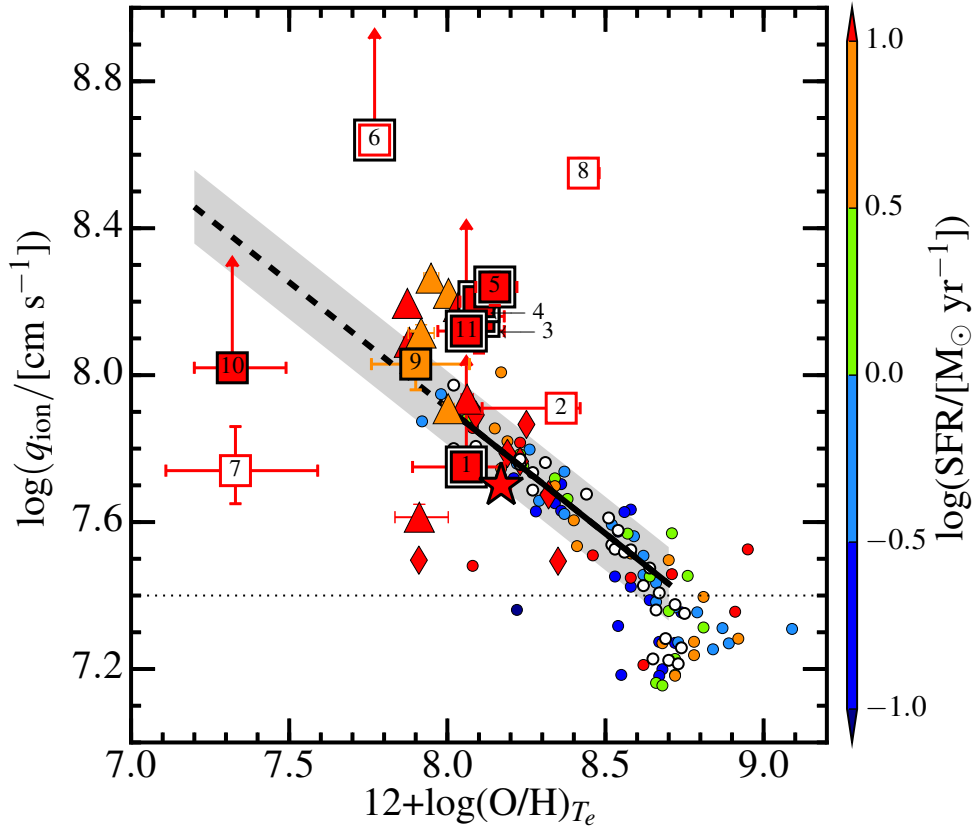


Fig. 11. $\log(q_{\text{ion}})$ as a function of $12 + \log(\text{O}/\text{H})_{T_e}$. The squares represent our $z \sim 2$ galaxies, while the filled squares show our $z \sim 2$ galaxies in the reliable sample. The squares with the arrows indicate the lower limits of q_{ion} at the 2σ levels. The star mark indicates the S16-stack. The circles show the local M_* -SFR stacks of Andrews & Martini (2013). The triangles and diamonds denote the local galaxies of GPs (Amorin et al. 2012; Jaskot & Oey 2013) and LMHSs (Section 5.2.2). All of the symbols, squares, circles, triangles, and diamonds have the color coding of SFR whose definition is the same as Figure 8. The $z \sim 2$ galaxies with $\text{EW}_0(\text{Ly}\alpha) > 20 \text{ \AA}$ are marked with the large black squares. The black solid line (the gray shaded region) indicates the best-fit linear function (the uncertainty) for the local M_* stacks. The black dotted line represents $\log(q_{\text{ion}}) = 7.4$, above which we perform the linear fitting. The black dashed line and the associated gray shade denote the extrapolation of the best-fit linear function and the 0.1 dex scatter in q_{ion} .

Table 6. ISM Properties of Galaxies

Objects (1)	q_{ion} excess (2)	N/O excess (3)	Class (4)
$z \sim 2$ galaxies			
S16-stack	no	yes	1)
ID-1 ^a , ID-5, ID-11	yes	no	2)
ID-3, ID-4	yes	yes	3)
local galaxies			
Reference galaxy	no	no	0)
3 LMHSs and 1 GP	no	yes	1)
3 GPs	yes	no	2)
1 GP	yes	yes	3)

(1): IDs or populations of Galaxies. (2): With and without a q_{ion} excess for "yes" and "no", respectively. (3): With and without an N/O excess for "yes" and "no", respectively. (4): Classifications; 0) for galaxies with neither N/O nor q_{ion} excess, 1) for galaxies with an N/O excess and no q_{ion} excess, 2) for galaxies with a q_{ion} excess and no N/O excess, and 3) for galaxies with both N/O and q_{ion} excesses.

^a A possible q_{ion} excess indicated by the lower limit on q_{ion} .

differences of $[\text{N II}]/\text{H}\alpha$ and $[\text{O III}]/\text{H}\beta$ values with the N/O and q_{ion} excesses by 0.3 dex from the reference galaxy. These N/O and q_{ion} excesses by 0.3 dex are roughly similar to those of the galaxies in 1), 2), and 3). In Figure 13, the cyan, light green, and magenta arrows indicate the $[\text{N II}]/\text{H}\alpha$ and $[\text{O III}]/\text{H}\beta$ differences that are estimated by our CLOUDY modeling. The cyan (light green) arrow corresponds to the N/O (q_{ion}) excess by 0.3 dex and the magenta arrow indicates both N/O and q_{ion} excesses by 0.3 dex. We confirm that these cyan, light green, and magenta arrows point to the positions of the 1), 2), and 3) galaxy groups, respectively. Thus, the positions of the 1), 2), and 3) galaxies can be explained by the excesses in N/O, q_{ion} , and N/O + q_{ion} , respectively.

In these arguments, we assume that all of the galaxies, our galaxies, S16-stack, GPs, and LMHSs, have exactly the same oxygen abundance of $12 + \log(\text{O}/\text{H}) = 8.10$. However, the oxygen abundances of these galaxies fall in the finite range of $12 + \log(\text{O}/\text{H}) = 8.10 \pm 0.15$. We examine how much the reference galaxy changes the position in Figure 13 for the oxygen

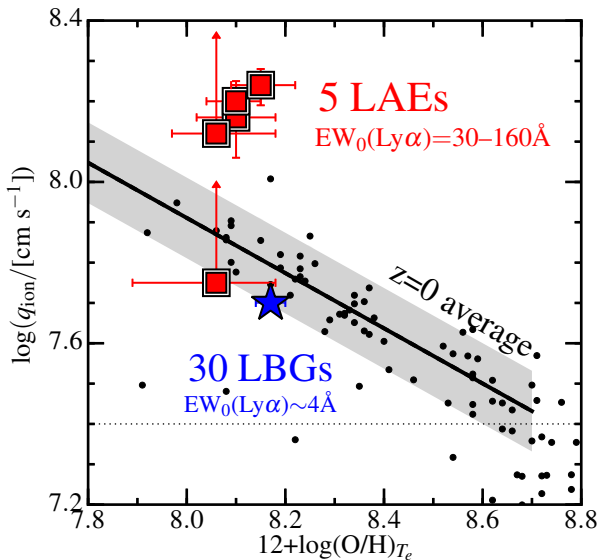


Fig. 12. Same as the bottom panel of Figure 11, but for the reliable galaxies with the measurements of $EW_0(\text{Ly}\alpha)$. The red and blue colors indicate galaxies with $EW_0(\text{Ly}\alpha) > 20\text{\AA}$ (classified as LAEs) and $EW_0(\text{Ly}\alpha) < 20\text{\AA}$, respectively.

abundances from $12 + \log(\text{O}/\text{H}) = 8.10 - 0.15$ to $8.10 + 0.15$. We make two CLOUDY models that are the same as the reference galaxy, but with the oxygen abundances of $12 + \log(\text{O}/\text{H}) = 8.10 - 0.15$ and $8.10 + 0.15$. We find that these two CLOUDY models give $[\text{N II}]/\text{H}\alpha$ and $[\text{O III}]/\text{H}\beta$ values that differ from the reference galaxy only by ~ 0.1 dex and ~ 0.03 dex, respectively. In Figure 11, we show these differences of the two models from the reference model with the black arrows. The oxygen abundance differences by ± 0.15 dex gives negligible changes in Figure 13.

We find that a large fraction of our $z \sim 2$ galaxies (ID-1, ID-5, ID-11, ID-3, ID-4, and the S16-stack) with BPT offsets have q_{ion} and/or N/O excesses, which are revealed by the direct T_e method, for the first time. Moreover, $z \sim 2$ galaxies with BPT offsets are not drawn from one of 1)–3) galaxy populations alone, but composed of 1)–3) populations.

We find that the 1)–3) population galaxies also exist at $z \sim 0$. However, these population galaxies are very rare in the local galaxies. In fact, we find that only less than 2,000 local galaxies indicate N/O or q_{ion} excesses in the 208,529 SDSS galaxies ($< 1\%$). These results suggest that 1)–3) population galaxies with BPT offsets emerge at $z \sim 2$ and mostly disappear in the present-day universe, except for local galaxies such as GPs and LMHSs.

6 SUMMARY

We have investigated the oxygen abundances (O/H), nitrogen-to-oxygen abundance ratios (N/O), and the ionization parameters (q_{ion}) for the eleven $z \sim 2$ galaxies and a stack made of

30 KBSS galaxies (dubbed “S16-stack”) with $[\text{O III}] \lambda 4363$ and $[\text{O III}] \lambda \lambda 1661, 1666$ lines. Our $z \sim 2$ galaxy sample includes Ly α emitters (LAEs) and Lyman break galaxies (LBGs). We have measured the O/H, N/O, and q_{ion} values by the direct T_e method, and studied the evolution of N/O and q_{ion} from $z \sim 0$ to $z \sim 2$. We have compared our $z \sim 2$ galaxies with the local stacks of the 208,529 SDSS galaxies and 9 GP galaxies, whose ISM properties are also measured by the direct T_e method. Our main results are summarized below.

- We have shown, for the first time, the relations of N/O- M_* and N/O-O/H for the $z = 0-2$ galaxies with the measurements by the direct T_e method. In the N/O- M_* relation (the top panel of Figure 9), the majority of the $z \sim 2$ galaxies have the N/O ratios comparable with (or lower than) the local sequence. In the N/O-O/H relation (the bottom panel of Figure 9), we find that there exist $z \sim 2$ galaxies with an N/O excess falling beyond the local sequence. For given O/H, our sample places the upper limit of N/O ratio $\log(\text{N}/\text{O}) \leq -1.26$ on average for $z \sim 2$ galaxies, suggesting that the N/O ratio does not increase largely (< 0.17 dex).
- We have compared the N/O values of the $z \sim 2$ and $z \sim 0$ galaxies in the same SFR and M_* ranges ($\log(\text{SFR}/M_\odot \text{ yr}^{-1}) > 1.0$ and $\log(M_*/M_\odot) = 9.0-10.0$). We choose our four $z \sim 2$ galaxies, the S16-stack, 206 SDSS galaxies (dubbed LMHSs), and four GPs. The N/O average of $z \sim 2$ galaxies and the S16-stack are comparable to or lower than those of GPs and LMHSs (Figure 10).
- We have presented, for the first time, the relation q_{ion} -O/H for the $z = 0-2$ galaxies with the measurements by the direct T_e method. We have identified that the seven out of our eleven galaxies at $z \sim 2$ have q_{ion} excesses at fixed O/H (Figure 11). These q_{ion} excesses are similar to those of some of the GPs in the local universe (Figure 11). In our reliable sample, the majority of $z \sim 2$ galaxies with $EW_0(\text{Ly}\alpha) > 20\text{\AA}$ indicate significant q_{ion} excesses, while the S16-stack ($EW_0(\text{Ly}\alpha) \sim 4\text{\AA}$) shows no q_{ion} excess (Figure 12). Thus we claim that q_{ion} excesses are related to high $EW_0(\text{Ly}\alpha)$ values.
- We have selected galaxies within $12 + \log(\text{O}/\text{H}) = 8.10 \pm 0.15$ and compared their loci on the BPT diagram (Figure 13). By fixing O/H values, we have resolved the degeneracies between N/O and q_{ion} on the BPT diagram. These $z \sim 2$ galaxies show BPT offsets, and the direct T_e method measurements indicate that these are 1) galaxies with an N/O excess and no q_{ion} excess, 2) galaxies with a q_{ion} excess and no N/O excess, and 3) galaxies with N/O and q_{ion} excesses, where the words of N/O and q_{ion} excesses are defined by the positive departures of N/O and q_{ion} measurements, respectively, from the local sequences for a fixed O/H. These results suggest that the BPT offsets at $z \sim 2$ are not made by one of 1)–3) galaxy populations alone, but the composite of 1)–3) populations. We identify that local galaxies of LMHSs and GPs

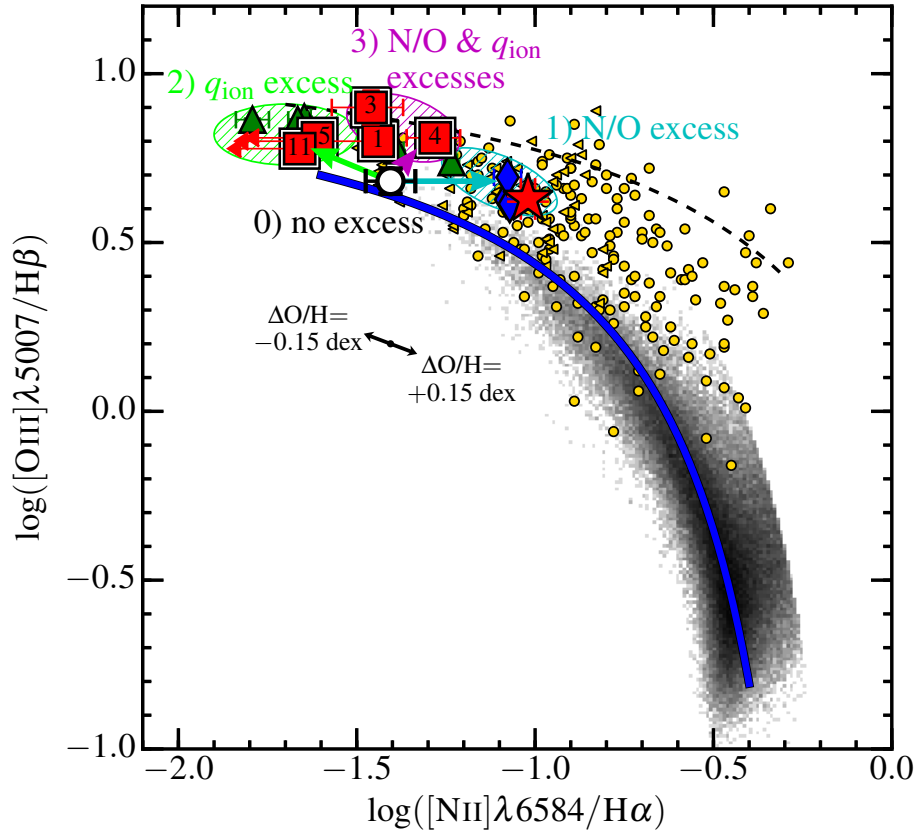


Fig. 13. Same as Figure 3, but for the five galaxies (red squares) and the S16-stack (red star mark). We compare the GPs (green triangles) and LHMSs (blue diamonds). All of these galaxies and the stack have similar O/H values falling in $12+\log(\text{O}/\text{H})=8.10 \pm 0.15$. The open circle represents the reference galaxy with $12+\log(\text{O}/\text{H})=8.10$ that shows neither N/O nor q_{ion} excess (see text). The $z \sim 2$ galaxies with $\text{EW}_0(\text{Ly}\alpha) > 20 \text{ \AA}$ are marked with the large black squares. The black arrows indicate the changes of the reference galaxy position when the oxygen abundances are increased/decreased by 0.15 dex which are calculated by the CLOUDY models. Here we also present the positions of the three groups of 1), 2), and 3) with the cyan, green, and magenta shades, respectively. The cyan, green, and magenta arrows indicate the differences of $\log([\text{N II}]/\text{H}\alpha)$ and $\log([\text{O III}]/\text{H}\beta)$ values given by our CLOUDY modeling for galaxies with 0.3 dex excesses of 1) $\log(\text{N}/\text{O})_{T_e}$, 2) q_{ion} , and 3) $\log(\text{N}/\text{O})_{T_e} + q_{\text{ion}}$, respectively, where we assume $12+\log(\text{O}/\text{H})=8.10$.

with BPT offsets similarly have 1)–3) properties. These local galaxies are probably counterparts of typical $z \sim 2$ galaxies.

- A large fraction of our $z \sim 2$ galaxies are classified as 1)–3) galaxies with N/O and/or q_{ion} excesses, while such N/O- and/or q_{ion} -excess galaxies are very rare in the local galaxies ($< 1\%$). These results would indicate that galaxies with the BPT offsets emerge at $z \sim 2$ and mostly disappear at $z \sim 0$, except for local galaxies such as GPs and LMHSs.

We thank the anonymous referee for constructive comments and suggestions. We are grateful to Mark Dijkstra, Dawn Erb, Andrea Ferrara, Tomotsugu Goto, Daichi Kashino, Lisa Kewley, Adam Leroy, Crystal Martin, Daniel Masters, Kentaro Motohara, Tohru Nagao, Masato Onodera, Ryan Sanders, Alice Shapley, Rhythm Shimakawa, Kazuhiro Shimasaku, Charles Steidel, Claudia Lagos Urbina, and Kiyoto Yabe, for their useful comments and discussions.

Funding for the SDSS and SDSS-II has been provided by

the Alfred P. Sloan Foundation, the Participating Institutions, the National Science Foundation, the U.S. Department of Energy, the National Aeronautics and Space Administration, the Japanese Monbukagakusho, the Max Planck Society, and the Higher Education Funding Council for England. The SDSS Web Site is <http://www.sdss.org/>.

The SDSS is managed by the Astrophysical Research Consortium for the Participating Institutions. The Participating Institutions are the American Museum of Natural History, Astrophysical Institute Potsdam, University of Basel, University of Cambridge, Case Western Reserve University, University of Chicago, Drexel University, Fermilab, the Institute for Advanced Study, the Japan Participation Group, Johns Hopkins University, the Joint Institute for Nuclear Astrophysics, the Kavli Institute for Particle Astrophysics and Cosmology, the Korean Scientist Group, the Chinese Academy of Sciences (LAMOST), Los Alamos National Laboratory, the Max-Planck-Institute for Astronomy (MPIA), the Max-

Planck-Institute for Astrophysics (MPA), New Mexico State University, Ohio State University, University of Pittsburgh, University of Portsmouth, Princeton University, the United States Naval Observatory, and the University of Washington.

This work is supported by World Premier International Research Center Initiative (WPI Initiative), MEXT, Japan, and KAKENHI (15H02064) Grant-in-Aid for Scientific Research (A) through Japan Society for the Promotion of Science (JSPS).

References

- Amorín, R., Pérez-Montero, E., Vílchez, J. M., & Papaderos, P. 2012, *ApJ*, 749, 185
- Amorín, R. O., Pérez-Montero, E., & Vílchez, J. M. 2010, *ApJ*, 715, L128
- Andrews, B. H., & Martini, P. 2013, *ApJ*, 765, 140
- Baldwin, A., Phillips, M. M., & Terlevich, R. 1981, *PASP*, 93, 817
- Bayliss, M. B., Rigby, J. R., Sharon, K., et al. 2014, *ApJ*, 790, 144
- Brinchmann, J., Charlot, S., White, S. D. M., et al. 2004, *MNRAS*, 351, 1151
- Brinchmann, J., Pettini, M., & Charlot, S. 2008, *MNRAS*, 385, 769
- Calzetti, D., Armus, L., Bohlin, R. C., et al. 2000, *ApJ*, 533, 682
- Campbell, A., Terlevich, R., & Melnick, J. 1986, *MNRAS*, 223, 811
- Cardelli, J. A., Clayton, G. C., & Mathis, J. S. 1989, *ApJ*, 345, 245
- Chabrier, G. 2003, *PASP*, 115, 763
- Charlot, S., Kauffmann, G., Longhetti, M., et al. 2001, *MNRAS*, 330, 876
- Christensen, L., Laursen, P., Richard, J., et al. 2012a, *MNRAS*, 427, 1973
- Christensen, L., Richard, J., Hjorth, J., et al. 2012b, *MNRAS*, 427, 1953
- Dere, K. P., Landi, E., Mason, H. E., Monsignori Fossi, B. C., & Young, P. R. 1997, *A&AS*, 125, 149
- Dopita, M. A., & Evans, I. N. 1986, *ApJ*, 307, 431
- Dopita, M. A., Kewley, L. J., Heisler, C. A., & Sutherland, R. S. 2000, *ApJ*, 542, 224
- Dopita, M. A., Fischera, J., Sutherland, R. S., et al. 2006a, *ApJ*, 647, 244
- Dopita, M. A., Fischera, J., Sutherland, R. S., et al. 2006b, *ApJS*, 167, 177
- Erb, D. K., Pettini, M., Steidel, C. C., et al. 2016, *ApJ*, 830, 52
- Erb, D. K., Shapley, A. E., Pettini, M., et al. 2006, *ApJ*, 644, 813
- Ferland, G. J., Korista, K. T., Verner, D. A., et al. 1998, *PASP*, 110, 761
- Ferland, G. J., Porter, R. L., Van Hoof, P. A. M., et al. 2013, *RMxAA*, 49, 137
- Fosbury, R. A. E., VillarMartin, M., Humphrey, A., et al. 2003, *ApJ*, 596, 797
- Garnett, D. R. 1990, *ApJ*, 363, 142
- . 1992, *AJ*, 103, 1330
- Garnett, D. R., Skillman, E. D., Dufour, R. J., et al. 1995, *ApJ*, 443, 64
- Groves, B. A., Dopita, M. A., & Sutherland, R. S. 2004, *ApJS*, 153, 9
- Hayashi, M., Ly, C., Shimasaku, K., et al. 2015, *PASJ*, 67, 80
- Hillier, D. J., & Miller, D. L. 1998, *ApJ*, 496, 407
- . 1999, *ApJ*, 519, 354
- Iwamuro, F., Moritani, Y., Yabe, K., et al. 2012, *PASJ*, 64, 59
- Izotov, Y. I., Guseva, N. G., & Thuan, T. X. 2011, *ApJ*, 728, 161
- Izotov, Y. I., Stasińska, G., Meynet, G., Guseva, N. G., & Thuan, T. X. 2006, *A&A*, 448, 955
- Izotov, Y. I., Thuan, T. X., & Guseva, N. G. 2012, *A&A*, 546, A122
- James, B. L., Pettini, M., Christensen, L., et al. 2014, *MNRAS*, 440, 1794
- Jaskot, A. E., & Oey, M. S. 2013, *ApJ*, 766, 91
- Kashino, D., Silverman, J. D., Sanders, D., et al. 2017, *ApJ*, 835, 88
- Kauffmann, G., Heckman, T. M., White, S. D. M., et al. 2003, *MNRAS*, 341, 54
- Kennicutt, R. C. 1998, *ARA&A*, 36, 189
- Kewley, L. J., & Dopita, M. A. 2002, *ApJS*, 142, 35
- Kewley, L. J., Dopita, M. A., Leitherer, C., et al. 2013a, *ApJ*, 774, 100
- Kewley, L. J., & Ellison, S. L. 2008, *ApJ*, 681, 1183
- Kewley, L. J., Maier, C., Yabe, K., et al. 2013b, *ApJ*, 774, L10
- Kimura, M., Maihara, T., Iwamuro, F., et al. 2010, *PASJ*, 62, 1135
- Kobulnicky, H. A., & Kewley, L. J. 2004, *ApJ*, 617, 240
- Kroupa, P. 2001, *MNRAS*, 322, 231
- Leitherer, C., Ekström, S., Meynet, G., et al. 2014, *ApJS*, 212, 14
- Leitherer, C., Ortiz Otlávaro, P. A., Bresolin, F., et al. 2010, *ApJS*, 189, 309
- Leitherer, C., Schaerer, D., Goldader, J. D., et al. 1999, *ApJS*, 123, 3
- Liu, X., Shapley, A. E., Coil, A. L., Brinchmann, J., & Ma, C.-P. 2008, *ApJ*, 678, 758
- Madau, P., & Dickinson, M. 2014, *ARA&A*, 52, 415
- Mannucci, F., Cresci, G., Maiolino, R., Marconi, A., & Gnerucci, A. 2010, *MNRAS*, 408, 2115
- Masters, D., Faisst, A., & Capak, P. 2016, *ApJ*, 828, 18
- Masters, D., McCarthy, P., Siana, B., et al. 2014, *ApJ*, 785, 153
- McCracken, H. J., Milvang-Jensen, B., Dunlop, J., et al. 2012, *A&A*, 544, A156
- McLean, I. S., Steidel, C. C., Epps, H. W., et al. 2010, *Proc. SPIE*, 7735, 77351E
- . 2012, *Proc. SPIE*, 8446, 84460J
- Nakajima, K., & Ouchi, M. 2014, *MNRAS*, 442, 900
- Nakajima, K., Ouchi, M., Shimasaku, K., et al. 2013, *ApJ*, 769, 3
- . 2012, *ApJ*, 745, 12
- Oke, J., Postman, M., & Lubin, L. M. 1998, *AJ*, 116, 549
- Oke, J. B., & Gunn, J. E. 1983, *ApJ*, 266, 713
- Onodera, M., Carollo, C. M., Lilly, S., et al. 2016, *ApJ*, 822, 42
- Osterbrock, D. E. 1989, *Astrophysics of gaseous nebulae and active galactic nuclei* (Mill Valley, CA: University Science Books)
- Overzier, R. A., Heckman, T. M., Tremonti, C., et al. 2009, *ApJ*, 706, 203
- Pauldrach, A. W. A., Hoffmann, T. L., & Lennon, M. 2001, *A&A*, 375, 161
- Peimbert, M. 1967, *ApJ*, 150, 825
- Pérez-Montero, E., & Contini, T. 2009, *MNRAS*, 398, 949
- Pérez-Montero, E., Hägele, G. F., Contini, T., & Díaz, Á. I. 2007, *MNRAS*, 381, 125
- Pérez-Montero, E., Vílchez, J. M., Cedrés, B., et al. 2011, *A&A*, 532, A141
- Pettini, M., Christensen, L., D’Odorico, S., et al. 2010, *MNRAS*, 402, 2335
- Pilyugin, L. S., Grebel, E. K., & Mattsson, L. 2012a, *MNRAS*, 424, 2316
- Pilyugin, L. S., Vílchez, J. M., Mattsson, L., & Thuan, T. X. 2012b, *MNRAS*, 421, 1624
- Pustilnik, S., Kniazev, A., Pramskij, A., et al. 2004, *A&A*, 419, 469
- Queyrel, J., Contini, T., Pérez-Montero, E., et al. 2009, *A&A*, 506, 681
- Salim, S., Rich, R. M., Charlot, S., et al. 2007, *ApJS*, 173, 267
- Salpeter, E. E. 1955, *ApJ*, 121, 161
- Sanders, R. L., Shapley, A. E., Kriek, M., et al. 2016, *ApJ*, 816, 23
- Seaton, M. J. 1975, *MNRAS*, 170, 475
- Shapley, A. E., Coil, A. L., Ma, C.-P., & Bundy, K. 2005, *ApJ*, 635, 1006
- Shapley, A. E., Reddy, N. A., Kriek, M., et al. 2015, *ApJ*, 801, 88
- Shaw, R. A., & Dufour, R. J. 1995, *PASP*, 107, 896
- Shibuya, T., Ouchi, M., Nakajima, K., et al. 2014, *ApJ*, 788, 74

- Shimakawa, R., Kodama, T., Steidel, C. C., et al. 2015, MNRAS, 451, 1284
- Shirazi, M., Brinchmann, J., & Rahmati, A. 2014, ApJ, 787, 120
- Skelton, R. E., Whitaker, K. E., Momcheva, I. G., et al. 2014, ApJS, 214, 24
- Stark, D. P., Richard, J., Siana, B., et al. 2014, MNRAS, 445, 3200
- Steidel, C. C., Shapley, A. E., Pettini, M., et al. 2004, ApJ, 604, 534
- Steidel, C. C., Strom, A. L., Pettini, M., et al. 2016, ApJ, 826, 159
- Steidel, C. C., Rudie, G. C., Strom, A. L., et al. 2014, ApJ, 795, 165
- Strom, A. L., Steidel, C. C., Rudie, G. C., et al. 2016, ArXiv e-prints, arXiv:1608.02587
- Trainor, R. F., Strom, A. L., Steidel, C. C., & Rudie, G. C. 2016, ApJ, 832, 171
- Villar-Martín, M., Cerviño, M., & Delgado, R. M. G. 2004, MNRAS, 355, 1132
- Yabe, K., Ohta, K., Iwamuro, F., et al. 2014, MNRAS, 437, 3647
- Yabe, K., Ohta, K., Akiyama, M., et al. 2015, PASJ, 67, 1
- York, D. G., Adelman, J., Anderson, J. E., et al. 2000, AJ, 120, 1579
- Yuan, T.-T., & Kewley, L. J. 2009, ApJ, 699, L161